LAWRENCE
LIVERMORE
NATIONAL
LABORATORY

Gaseous Laser Targets and Optical Dignostics for Studying Compressible Turbulent Hydrodynamic Instabilities

M. John Edwards, J.F. Hansen, Aaron R. Miles, D.H. Froula, G. Gregori, S.H. Glenzer, A.D. Edens, T. Dittmire

February 14, 2005

Disclaimer

FY04 LDRD Final Report
Gaseous Laser Targets And Optical Diagnostics For Studying Compressible Turbulent Hydrodynamics
LDRD Project Tracking Code: 02-ERD-023
John Edwards, Principal Investigator

Abstract

The possibility of studying compressible turbulent flows using gas targets driven by high power lasers and diagnosed with optical techniques is investigated. The potential advantage over typical laser experiments that use solid targets and x-ray diagnostics is more detailed information over a larger range of spatial scales. An experimental system is described to study shock – jet interactions at high Mach number. This consists of a mini-chamber full of nitrogen at a pressure ~ 1 atms. The mini-chamber is situated inside a much larger vacuum chamber. An intense laser pulse (~100J in ~ 5ns) is focused on to a thin ~ 0.3μm thick silicon nitride window at one end of the mini-chamber. The window acts both as a vacuum barrier, and laser entrance hole. The "explosion" caused by the deposition of the laser energy just inside the window drives a strong blast wave out into the nitrogen atmosphere. The spherical shock expands and interacts with a jet of xenon introduced though the top of the mini-chamber. The Mach number of the interaction is controlled by the separation of the jet from the explosion. The resulting flow is visualized using an optical schlieren system using a pulsed laser source at a wavelength of 0.53 μm. The technical path leading up to the design of this experiment is presented, and future prospects briefly considered. Lack of laser time in the final year of the project severely limited experimental results obtained using the new apparatus.

1. Introduction

Compressible turbulent mixing is a complex subject with many unresolved questions and will remain an active area of study for many years. For example there is as yet no firm consensus as to the role of initial conditions or compressibility on the evolution of a mixing region driven by the classical Rayleigh-Taylor instability[1], and current state of the art simulations predict values for growth rates that are different from experiment [2]. Another important question concerns what is typically referred to as the intensification of turbulence due to shock-turbulence interaction in for example shock-jet collisions [3-5] or the passage of a shock through an existing mixing region [6,7]. It is known that the passage of shocks through already turbulent flows substantially changes the velocity fluctuations and length scales, which will likely impact the mixing process [3]. Typically there is agreement that velocity fluctuations (and therefore turbulent kinetic energy) increase, but there are contradictory results from experiment and simulation on the evolution of length scales in the post shock flow [3,8]. Amplification is predicted to saturate for mach numbers, M>3 [8], but experiments exist almost exclusively in the incompressible regime (M~1) [3].

Most of the experimental work at low Mach number has been conducted in shock tubes or other devices that use gases, and such flows can now be readily diagnosed by a suite of extremely powerful optical, and electro-mechanical diagnostics, which provide a wealth of detailed information about the flow fields [see eg 9-11]. On the other hand, most work on highly compressible systems has been confined to energetic drivers such as lasers using targets that are nearly always close to solid density [12-15]. As a result, it is necessary to use X-rays to image the flow. The line of sight integration inherent to X-ray shadowgraphy, and the limited spatial resolution available (~ 10 μm) with current diagnostics confine useful information to gross structures, which are nearly always modeled well by sophisticated radiation hydrocodes [13].

The work presented here is concerned with the development of a new technique to access the compressible, high Mach number regime, initially in shock-jet interactions. The approach being pursued is to use a laser driver in combination with gaseous targets and optical diagnostics in order to improve the diagnosability of high Mach number laser experiments. This comes about, both because low-density targets admit the use optical diagnostics, and also because lower density targets translate directly to larger spatial scales. The net result is that it should be possible to resolve a larger range of scales in this new class of system compared to the more traditional laser experiment. For simplicity, the shock wave is provided by a laser driven blast wave propagating in nitrogen, and the primary interaction medium is a jet of xenon. The principle diagnostic to image the flow field is schlierien photography [16] using a pulsed coherent source, although an interferometer and spectrometer were also used to characterize blast wave evolution.

The paper is arranged as follows. Background information on laser driven blast wave characteristics, scaling, and potential benefits for gas targets compared to solid targets are quantified in section 2. Section 3 describes experiments to study and characterize laser driven blast wave formation and evolution. Initial interaction studies are presented in section 4, and followed by a description of improvements for the next generation of experiments in section 5. The results of these experiments

are presented in section 6, and a post mortem carried out in section 7, followed by the exit strategy in 8. A break down of laser shot time is given in appendix 1.

2. Laser driven blast wave characteristics

To generate a spherical blast wave using a laser, the pulse of light is typically focused on to a target surrounded by an ambient gas[17,18]. Most of the light is absorbed and coupled into the target, which ablates at high velocity creating the miniature explosion characteristic of a classical blast wave. Because the laser has to propagate through the gas in this configuration, the initial gas density must remain below a certain value so as to avoid laser break down, and energy dissipation prior to the pulse reaching the target. This depends mainly on the laser intensity and gas, but also somewhat on the beam characteristics. This initial background pressure, or density limitation turns out to have significant implications for diagnostics, and has motivated a new target geometry that will be described later. At the other end of the density scale, the continuum approximation eventually breaks down in the plasma created by the blast wave. This has been estimated to begin for background gas pressures below ~ 1/1000th atms in nitrogen [17], which is well below the lowest backing pressures considered in this work.

Other considerations when using laser drivers include target material and geometry, as well as gas composition. High Z targets are known to convert a significant fraction of their energy into X-rays[19,20], which, depending on the absorption length in the surrounding gas, might escape or produce significant preheating prior to shock arrival. A substantial escape of energy would be undesirable, and was not found to be significant for a number of target materials considered coupled with the background gas pressures used here. The ability to control preheating may be beneficial for altering the initial conditions in interaction object, but was not pursued significantly in this study. These topics are discussed in more detail in section 3.

The details of the initial blast wave formation are largely irrelevant to the asymptotic evolution of the wave. What matters is the energy deposited and the initial ga density through which the wave expands, and to a lesser extent the equation of state of the material. The evolution of a simple (Sedov-Taylor) spherical blast wave is a well understood classical problem [21]. The asymptotic trajectory of the shock front is given by

$$R = \alpha t^{2/5} \quad ; \quad \alpha = \left[\frac{4}{\pi} \frac{(\gamma+1)^2(\gamma-1)}{3\gamma-1} \right]^{1/5} \left(\frac{E}{\rho} \right)^{1/5}$$

where γ and ρ are the adiabatic index and density of the gas respectively, and is E the deposited energy. This is independent of the laser intensity, which only influences the early time expansion of the wave. The asymptotic relation becomes a very good approximation once the blast wave has swept up a mass equivalent to the mass contained in the initial explosion. Rearranging this expression, the radius at which the leading shock front attains a given velocity, v, can be written as

$$R_V = \left(\frac{2}{5}\right)^{\frac{2}{3}}\left[A\left(\frac{E}{\rho}\right)\right]^{\frac{1}{3}} V^{-\frac{2}{3}} \approx 10^4 \left(\frac{E_{joule}}{\left[n_{per\,cc}/10^{18}\right]A}\right)^{\frac{1}{3}} V_{cm/s}^{-\frac{2}{3}} \quad cm$$

where n is the particle density and A the molecular weight (~30 for air). The sound speed of air, which is mostly nitrogen, at room temperature is $\sim 3\times10^4$ cm/s, and a shock moving at Mach 10 would have a speed $\sim 3\times10^5$ cm/s. If we take E $\sim$ 100 J, (which corresponds to a laser such as the current Janus system at LLNL), a background gas number density $\sim 10^{18}$ per cc (~1/20th atms), we see from the above relation that the wave would have slowed to Mach ~10 at a radius ~ 3cm, which is considerably larger than typical laser hydrodynamics experiments. For a 10 kJ system such as the Omega laser, this translates to $\sim$ 10 cm, and to $\sim$ 1 m for the NIF. Increasing the gas density to $\sim 2\times10^{19}$ per cc ($\sim$ 1 atms) reduces all scales by about a factor of 2.7. This is instructive because diagnostics become much easier as the background density increases, and it turns out that future experiments will likely operate at close to 1 atmosphere. To be more explicit regarding the Mach number scaling we note that V~M, and the above expression can be rearranged to give

$$M \approx 30 \left(\frac{E_J}{\left[n_{per\,cc}/10^{18}\right]A}\right)^{\frac{1}{2}} R_{cm}^{-\frac{3}{2}}$$

Written this way, the potential size benefits compared to solid experiments become very obvious. For a given facility, it is just the square root of the ratio of the initial densities $\sim$ 50. With the same diagnostic resolution typical of solid experiments using X-ray backlighting ($\sim$ 10-20 μm), this translates to being able to resolve a range of scales in the flow $\sim$ 50x larger in the gas experiment, or typically a range of scales of $\sim$ 500. When this is coupled to the potential to routinely obtain resolutions $\sim$ 5μm or less the range of scales in the flow that might be observable is in the range of $\sim$ 1000. The significance of this is that the upper and dissipative scales begin to become decoupled when the range of scales is $\sim$ 1000, allowing an inertial range to be established, triggering a turbulent mixing transition [ref 21 presents convincing evidence for a wide variety of flows that suggest transition occurs at Re $\sim$ 2×10^4, which corresponds to a range of scales $\sim$ 1700). On the down side, the approach presented here is obviously only easily applied to certain target configurations such as the one we describe in detail later. Solid experiments will remain attractive because, unlike in gas experiments, it is possible to control precisely the initial geometry.

Finally, the degree to which the relative spatial resolution improvement can be taken advantage of in gas experiments will depend on the diagnostics that can be developed. The Schlieren system used for this study provides much more information than a typical X-ray shadowgram, but more advanced diagnostics may be possible. To see this, it is instructive to consider the temperature behind a M~10 shock wave traveling through air initially at room temperature. For such a high Mach number the pressure ratio at the shock is approximately 2 $\gamma M^2/(\gamma+1)$~M^2 for air with γ ~1.4. The compression through the shock is $\sim$ 6 and the temperature increase is therefore a factor of ~10-15 corresponding to a temperature $\sim$ 1/2 eV. This is low enough that optical pumping of transitions for advanced diagnostic systems remains a possibility, but this is not discussed further here.

3. Blast wave characterization

3.1 Blast waves in nitrogen

We created spherically expanding blast waves in the following fashion: a high-power infrared pulsed laser (1064 nm wavelength) is focused onto a small piece of solid material, typically the tip of a pin, but we also tried foils (see below). The solid is surrounded by an ambient gas typically at a pressure of ~1 kPa (~ 1/100 atms). The laser pulse (5 ns duration and energy ranging from ~1 J to ~150 J) ablates the solid and rapid expansion of ablated material shocks the ambient gas. The initial shock travels radially outward, collecting ambient gas in a shell immediately behind the shock front. To image a blast wave on spatial scales up to ≈5 cm , we use two lenses in a telescope configuration and a gated, single-frame, high-speed CCD camera (2 ns gate), along with a low energy, green laser pulse (532nm wavelength, 15 ns duration) as a backlighter. Blast wave radius as a function of time is obtained by employing a schlieren technique so that only laser light perturbed by the plasma is imaged; light which has not been deflected is removed at the telescope focal point by a small (≈500μm) beam block. With this method, image brightness corresponds to the spatial derivative of plasma electron density, and the blast wave structure is readily seen. Schlieren images were obtained from 5 ns up to 35μs after the initial, laser pulse (see Fig. 1).

Figure 1. Schlieren images of blast wave expansion through ambient nitrogen gas (1.3kPa) at times t=150ns to 6μs after an ablative laser pulse (energy E=10J , duration 5ns) is focused on a solid pin (visible in images, pointed down). The laser pulse was incident from the left. The shock is spherical (except on the laser side due to laser-plasma interaction) and its growth is consistent with a Taylor-Sedov blast wave. The image to the right (t=150ns to 6μs) is a composite of four images (with overlapping pin locations).

The blast wave velocity drops as more and more of the ambient gas is accumulated and set in motion by the passing shock. Once more mass has been swept up by the shock than what was initially present, the shock could be regarded as without characteristic length or time scales, and so one would expect the well-known self-similar motion of a Taylor-Sedov blast wave, $r \sim t^{2/5}$, where r is shock radius and t is

time. This is precisely what we observe when using nitrogen gas as the ambient gas. Figure 2 shows the blast wave evolution in nitrogen.
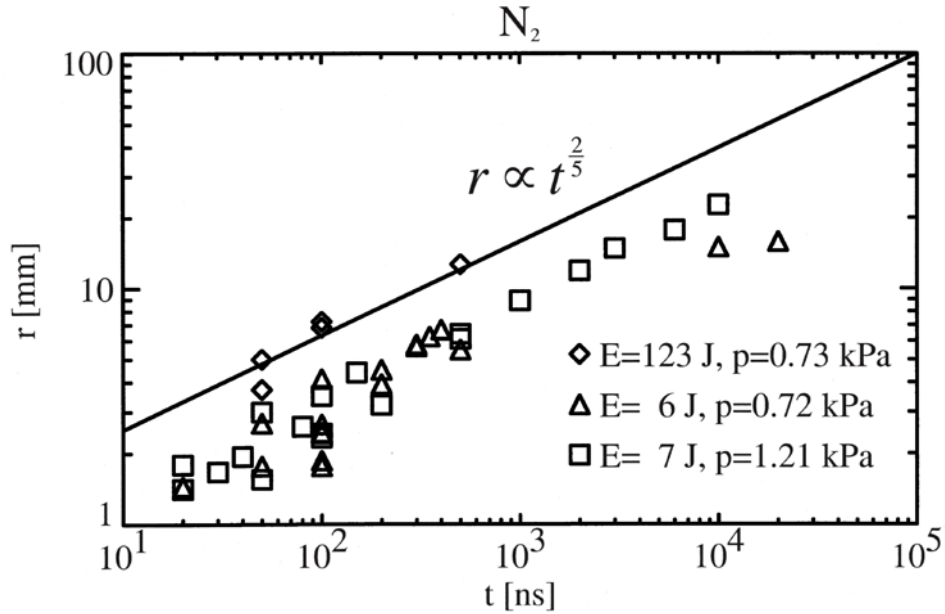
Figure 2. Blast wave radius as a function of time for three different data series (different combinations of laser energy and ambient gas pressure) for laser shots on a stainless steel pin in ambient nitrogen gas. The blast waves appear to follow Taylor-Sedov's relationship $r \sim t^{2/5}$.

From our schlieren data we can also plot blast wave radius r as a function of either the laser energy E or the ambient gas density r (see example in Fig. 3), and found this consistent with another aspect of the Taylor-Sedov relationship for blast waves, namely $r \sim (E/\rho)^{1/5}$. The Janus facility energy readings were calibrated with a Keithley calorimeter and were found to be accurate to within 10%. We also established that typically less than 5% of the energy passes by the target pin. (This could happen due to imperfect laser alignment.) The pressure readings from the target chamber baratron gauge were found to be accurate to within 10 Pa.
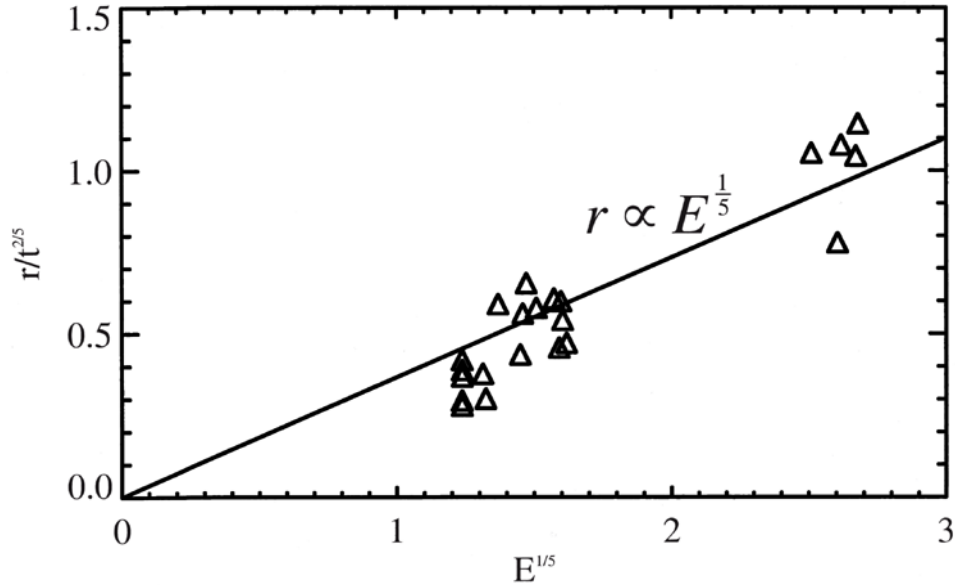
Figure 3. Blast wave radius (normalized by time to the two fifth power) as a function of laser energy to the one fifth power (all units in SI-units). The laser target was a stainless steel pin, and the ambient gas was nitrogen with a pressure p=0.73 kPa..

3.2 Blast waves in xenon

Strong blast waves in xenon (or indeed mixtures of nitrogen and xenon) were expected to behave differently from those in nitrogen because of significant radiative effects [17,23,24]. Experiments were conducted to explore the possibility of radiation from the blast wave being used to precondition an interaction medium. In the event, it was found that the blast wave shock was too radiative to be useful, driving strong blast waves off of any interaction object. However, the experiments lead to the discovery of a new and unexpected phenomena not previously considered in the literature. The initial shock being strong enough to be supercritical sends out a supersonic radiation wave ahead of itself. The new realization was that this radiation wave can effectively become decoupled from the original shock which rapidly weakens. Before the radiation wave can be caught by the shock, it becomes subsonic sending out a shock wave of its own which the first shock chases. Images of this sequence are shown in Fig 4. The "glow" surrounding the shock at early time (50-400 ns) is the supersonic heat wave. The frame at 1μs shows that the initial shock has become almost undetectable. The second shock is just discernible by 4μs and is clearly visible thereafter. See appendix 2 for a fuller discussion of these results.

Figure 4. Blast wave expansion through ambient xenon gas (p=1.3 kPa) at times t=50 ns to 30μs after an ablative laser pulse (energy E=10 J , duration 5 ns) is focused on a solid pin (visible in images, pointed down; pin location in bottom row of images is at the left edge of each image). The laser pulse was incident from the left. The initial shock is strongly radiative (super-critical) and preheats the ambient gas. At t=150 ns both the initial shock and the preheated gas ahead of it are clearly visible. At t≈1μs the initial shock begins to dissipate, and the shock front is no longer obviously sharp. At t≈4μs a second shock appears (located at tip of arrow), ahead of the initial shock. The second shock continues to expand while the initial shock gradually becomes undetectable. The final image (t=8μs , 30μs) is a composite of two images (with overlapping pin locations).

3.3 Electron density measurements

To measure the electron number density, we split the green laser beam into image and reference beams which are then recombined (after the image beam has passed through the plasma) in either a Michelson or a Wollaston interferometer. Density profiles $n_e(r)$ are then obtained from Abel inversions.

The interferometry data proved difficult to interpret correctly simply because the fringe shift at the shock is more than one fringe, and this shift occurs over a very small spatial scale.
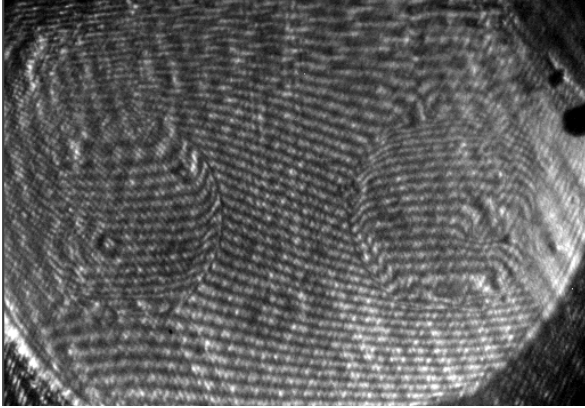
Figure 5. Wollaston interferogram of blast wave propagating in xenon (p=0.7 kPa). The deposited laser energy E=123 J has created a shock with radius r=5.2 mm at this time (t=100 ns). Note how the Michelson technique due to mirroring overlaps the fringes from both image and mirror image, and how this makes it difficult to interpret the actual fringe shift. Also note that the shock is so strong that multiple fringe shifts occur right at the shock boundary.

Ahead of the shocks, gradual fringe shifts over longer spatial scales are clearly visible in xenon, but absent in nitrogen, indicating preheated gas (plasma) ahead of the shock in xenon. The preheated portions extends so far ahead of the shocks that initial interferograms obtained with the Wollaston method included a doubling of the fringe shift where image and mirror image overlapped. To overcome this problem we rebuilt the interferometer from Wollaston to Michelson. The michelson interferometer does not create a mirror image, so there is no doubling of the fringe shifts, but the issue of multiple fringe shifts at the shock boundary remains. An attempt to Abel invert a Wollaston interferometer image can be seen in Fig.6.
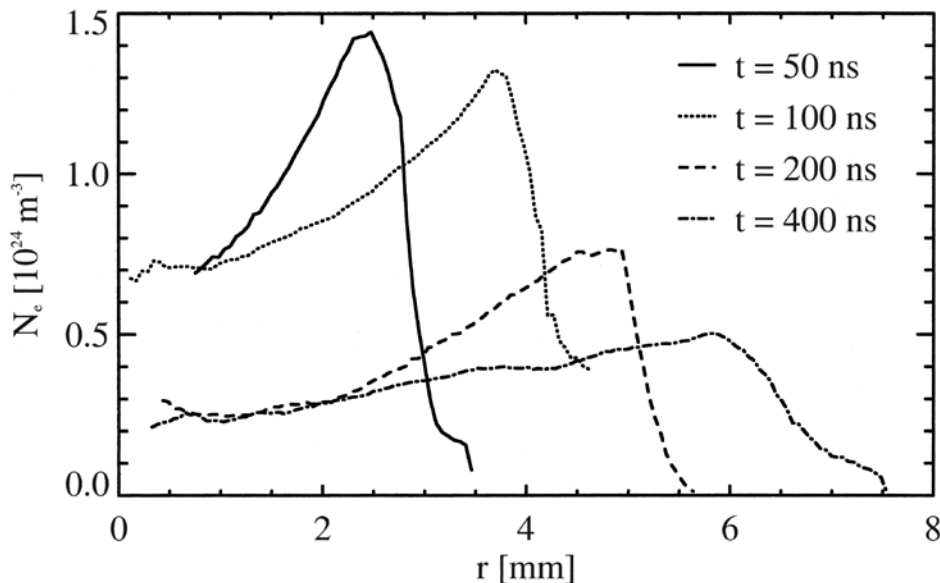
Figure 6. Density profiles calculated from Abel inversion of interferograms of four different blastwaves created by laser energies between E=6.6J to 10.6 J and propagating in nitrogen (p=0.7 kPa).

3.4 Specrtoscopic measurements

A 0.67 m, 2041 grooves/mm spectrometer was used in first order to obtain spectral line intensity as a function of position (both behind and ahead of the blast wave). Spectrograms were then Abel inverted to get spectral line intensity as a function of radius, and temperature as a function of radius was then estimated from pair-wise line ratios.

In nitrogen, emission spectroscopy data in the near ultraviolet range was readily obtained at and behind the blast wave in nitrogen, but no readings discernible from noise were possible ahead of the shock. Two temperature distributions calculated from pair-wise line ratios of two NII lines (399.5 nm and 444.70 nm) and two NIII lines (451.485 nm and 463.413 nm) generally agreed with each other except for a constant offset of ~1-2 eV (presumably from measurement error and from non-LTE effects). Figure 7 shows an example spectra taken at a time t=150 ns after the initial laser pulse (E=10J), with electron temperatures in the range 4 eV to 7 eV at and behind the shock. We see no signs of pre-heated gas ahead of the shock, suggesting that radiative effects are minimal.
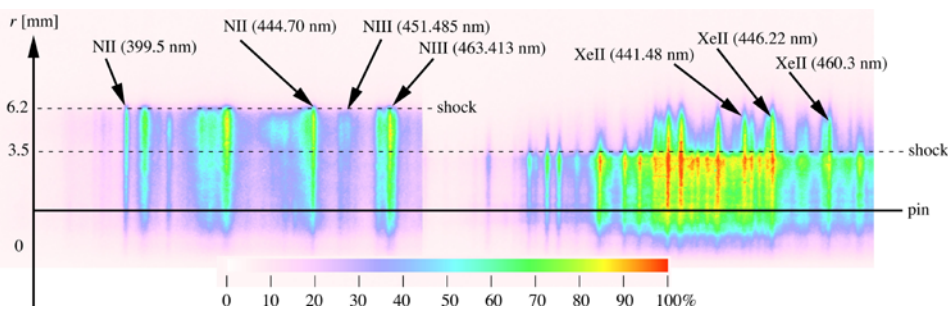
Figure 7. Spectra for nitrogen (left) and xenon (right) at t=150 ns . The location of the pin is marked with a solid line. The shock locations, as obtained from schlieren images, are indicated by dashed lines at radii r=6.2 mm for nitrogen and r=3.5 mm for xenon.

In xenon, spectroscopy data show that the temperature immediately ahead of the initial shock is roughly the same as behind it. A few millimeters in front of the shock the temperature then drops sharply (to noise levels). For example, at t=150 ns and a laser energy of E=10 J (see Fig. 7), the temperatures in the xenon case were in the range 1.6eV to 3.6eV, calculated from pair-wise line ratios of three XeII lines, 441.48 nm , 446.22 nm , and 460.3 nm. From measured temperatures, radii, and velocities, and a deduced (using a screened hydrogenic model) average ionization of 5.6, we calculate that the initial energy is distributed so that 52%-90% is in the preheated gas, 8%-22% is heat and internal energy in and behind the shock, and 4%-31% is kinetic energy; errors depend on uncertainties in temperature and locating the exact boundary of the preheated gas.

3.5 Blast wave asymmetry

It is evident from images of the blast wave evolution in Figs1,4 that there exists a significant asymmetry towards the laser side of the blast wave particularly in xenon. The asymmetry is partly due to the fact that the preferred initial expansion is along the laser beam, causing deviation from sphericity early in time, and a center to

the expansion that is off-set from the original pin location. In xenon, there is an additional pronounced effect. Weak laser heating via multi-photon ionization and then inverse bremsstrahlung absorption occurs as the beam propagates towards the target leading to the formation of a cylindrical blast wave expanding perpendicular to the beam direction [18, see Appendix 3]. The spherical wave then expands into the expanding cylindrical wave. Along the center of the cylindrical wave the density is relatively low, and the shock from the pin travels faster there. Conversely it is impeded in the region of the thin shocked expanding cylindrical shell. This leads to the characteristic shapes seen in the photographs at early time.
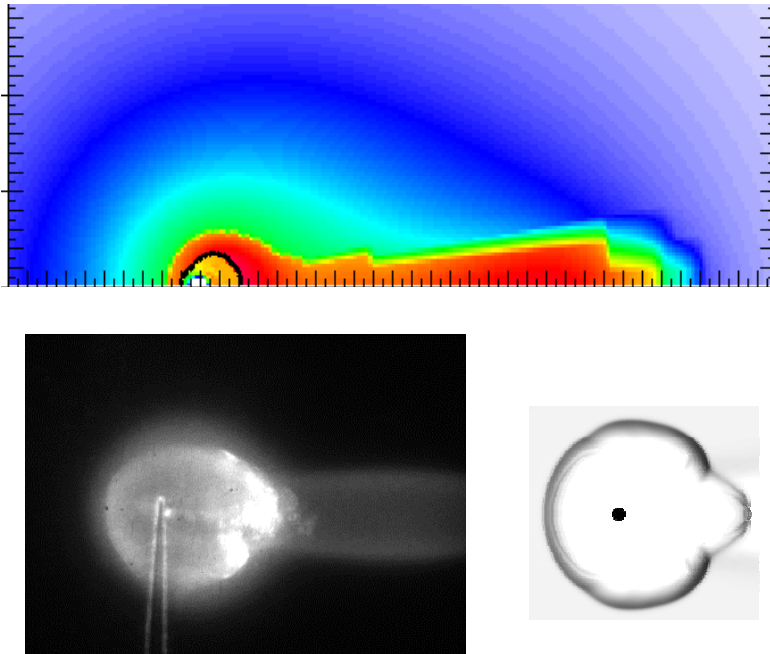
Figure 8. CALE simulation (Te) of a blast wave in xenon gas showing the development of a cylindrical blast wave out in front of the target due to laser deposition (top). The spherical blast wave is distorted as it propagates into this (experiment lower left; simulated density lower right).

3.6 Foil targets

Initial studies also used thin plastic foils ~ 2µm thick, supported on a small washer as the blast wave target. Blast wave evolution was studied on the rear side of the foil where an interaction object would be placed. In these preliminary experiments the object was a solid steel rod ~ 1mm diameter. Very energetic, clean shock waves were observed when the background gas was nitrogen, and the Schlieren imaging showed intricate detail of the shock-rod interaction(Fig 9). Unfortunately, reproducing such clean shocks later turned out to be very difficult, probably because of substantial variability in the mounting of the foil on the washer. In contrast, pin targets gave extremely reproducible results, and we therefore selected these or future development work despite the slightly lower coupling efficiency into the rearward direction.

–13–

In xenon gas we were never able to produce clean shocks, which we attribute to the radiative nature of the gas altering the early time hydrodynamics of the foil explosion and amplifying perturbations (Fig 9).
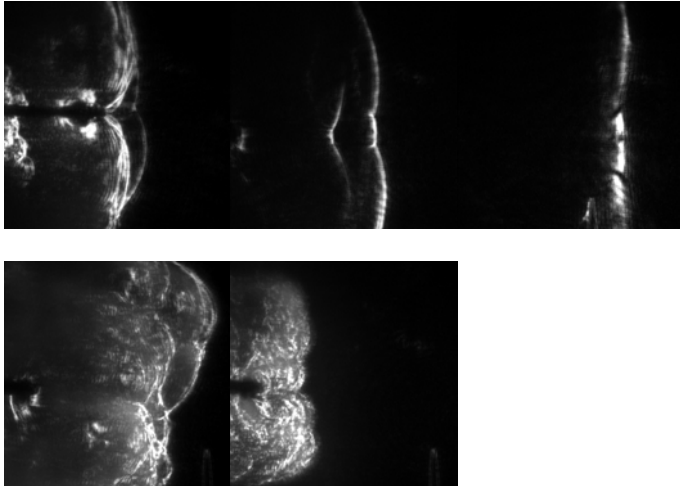
Figure 9. Schlieren image time sequence (top) of blast wave in nitrogen produced from laser interaction with a thin plastic foil (laser incident from left). The blast wave is distorted as it rolls over a rigid rod, which is held horizontally perpendicular to the plane of the images. Lower left: a more typical image in nitrogen when using foil targets; blast wave exhibits significant structure. Lower right: reproducible image of same case but in xenon.

3.7 Gas density limits imposed by laser breakdown

Diagnostic contrast is improved as the gas density (pressure) in increased allowing more detailed information to be extracted from the data. Unfortunately, the ambient gas pressure cannot be increased arbitrarily in this configuration, because eventually a point is reached where the laser can no longer propagate without breaking down the gas. We established this limit in a series of laser shots by gradually increasing the gas pressure until breakdown was observed, and found that the upper limit for propagating "rod shots" (a low energy shot which requires a relatively short laser cool-down before the next shot; E≈1 to 10J) in nitrogen without breakdown was ~8 kPa. For "system shots" (a high energy shot which requires a longer cool-down period; E≈100J to 150J) in nitrogen the limit was ~5.5 kPa. When the limit was exceeded, we typically observed a string of blast waves aligned with the laser focal cone (see Fig. 10).
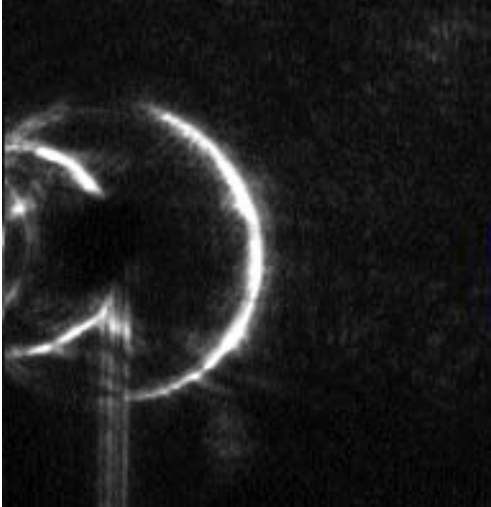
Figure 10. Schlieren image showing three blast waves in nitrogen gas with a pressure p=10.7 kPa. The blast waves were created by a laser beam incident from the left. The largest blast wave is centered on the tip of a target pin, indicating that most of the laser energy (E=3.3 J) was deposited there. However, the presence of the two smaller blast waves mean that some laser energy was deposited directly into the nitrogen gas ahead of the pin; the relatively dense gas cannot support laser propagation without breaking down.

4. Initial blast wave interaction experiments

4.1 Blast wave gas jet interactions

Initial blast wave – jet interactions used an existing gas injection system, designed to be used in vacuum for laser plasma interaction experiments, and as such was only able to operate with a high backing pressure. This system was used to inject a nitrogen jet with a 5.5 MPa back-pressure into a background of 0.9 kPa nitrogen. A short cylindrical nozzle was added to this system to improve the collimation slightly.

Figure 11. Schlieren time sequence of nitrogen shock-jet interaction taken over three separate shots (jet pressure is p_{jet}=5.5 MPa and the ambient gas, also nitrogen, is p=0.9 kPa). The jet, which is traveling vertically, can just be made out. The inset image shows just the jet flow (taken at atmospheric pressure for clarity) without the nozzle to show the turbulent structure of the jet. At the high jet pressure used in these experiments, the flow rapidly expands sideways as it exits the nozzle (see section 5). This is not readily seen directly, but is obvious from the interaction location in the first image.

Figure 11 shows a time sequence of shock jet interaction taken over three separate shots with nitrogen background gas and a nitrogen jet. The interaction is clearly evident in each image, but little detailed information can be seen. Xenon jets showed up better than nitrogen ones (Fig. 12) but the improvement in contrast and detail was not adequate for high quality flow studies. While more detail would be observable by increasing the magnification of the imaging system, the overall image quality strongly motivated improving the signal to noise levels substantially. As a result a new experimental arrangement, which we describe in section 5, was designed.
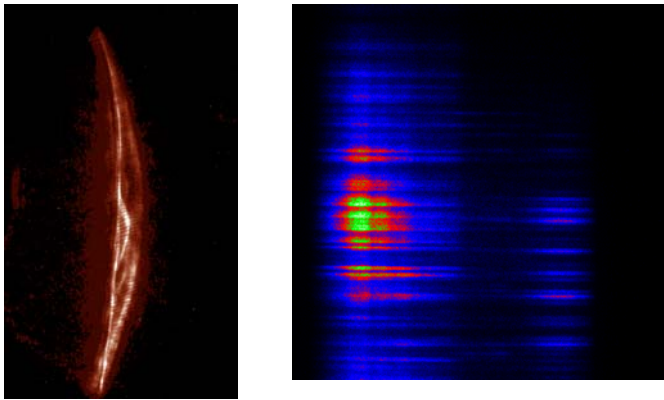
Figure 12. Schlieren image and spectrogram of nitrogen shock - xenon jet interaction. The interaction is qualitatively different from that in the nitrogen jet.

It is interesting to note that the shock-jet interaction is qualitatively different for the xenon jet; sharper, and a larger number of shell like structures can bee seen. This is likely the result of higher compressibility in the case of xenon due to ionization and radiative effects. It was also demonstrated that spectroscopic data could be obtained, which should provide useful information in later experiments. These data were not reduced further at this time.

A small set of interaction experiments was carried out using low density foam balls, and secondary blast waves, but turn out to be of little interest for these purposes and were not pursued further (see appendix 4).

5. Design of a high pressure experimental system

5.1 Numerical studies of jets

The gas jet used in the first exploratory studies was designed to be used in vacuum for laser plasma interaction studies, and as such had an extremely high backing pressure. This results in a highly turbulent flow, and the very large over pressure causes a rapid expansion of the gas flow in any surrounding medium

thereby reducing its diagnosability. In principle, small over pressures should suffice to produce well collimated flows [25], but the particular gas jet could not operate in this regime. Prior to specifying a new design, jet flow was explored in a simple geometry using the second order Godunov, Adaptiev Mesh Refinement code, Raptor[26]. A variety of configurations was studied, from large to small reservoirs, for a variety of ambient to reservoir pressures. Several example results are shown in Fig. 15.
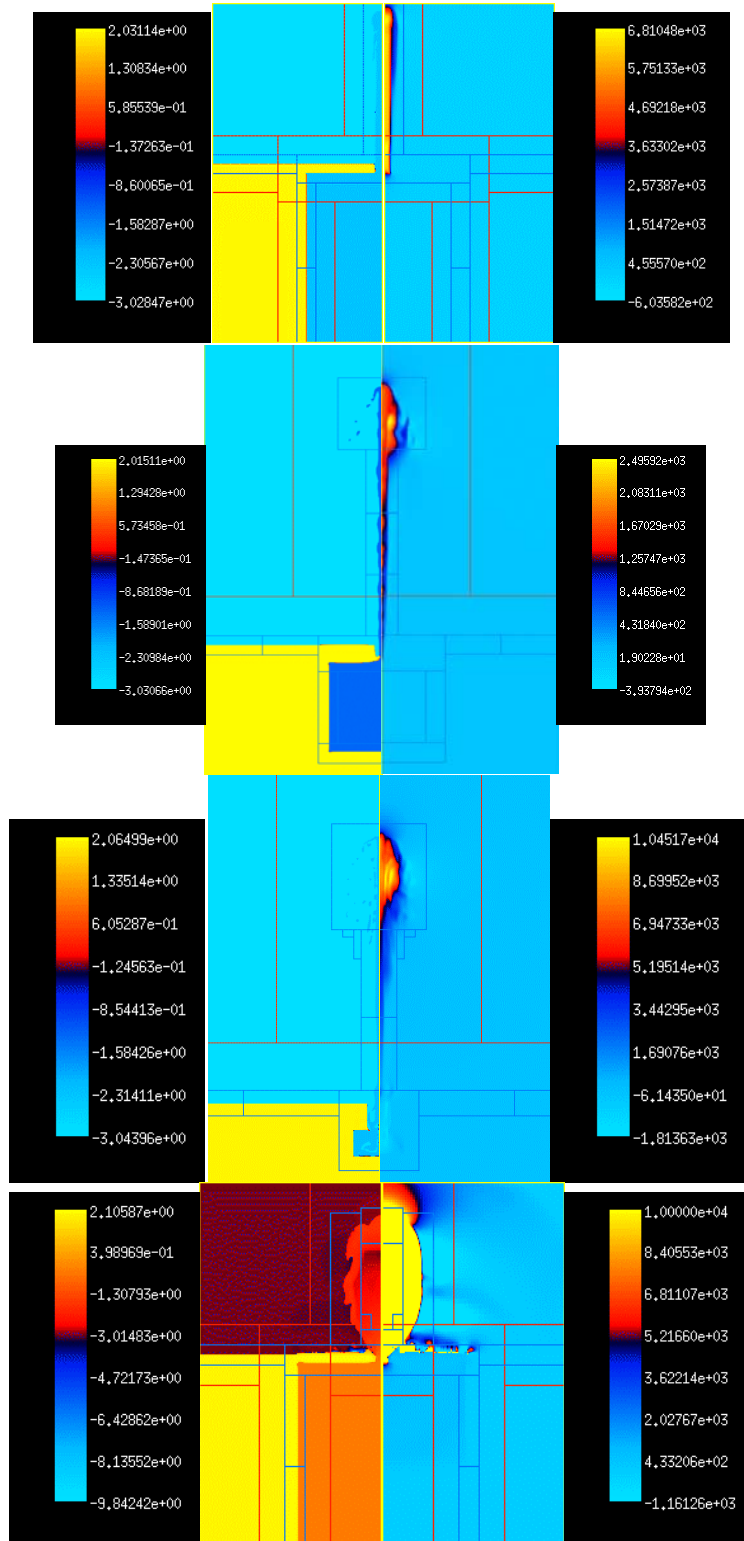
Figure 13. Snapshots of gas jets predicted by Raptor for a variety of configurations. The ambient gas is nitrogen at 1 atmosphere, and the jet gas is xenon. The left hand figure is $\log_{10}$(density g/cc), and the right figure is vertical velocity (cm/s). From top to bottom: 1)reservoir pressure, P_R=1.1 atms, opening=1x1mm, time = 0.46ms; 2) P_R=1.1 atms, opening=0.5x1mm, time = 1.0ms; 3) P_R=2 atms, opening=0.5x1mm, time = 0.15ms; P_R=100 atms, opening=1x1mm, time = 0.065ms.

In all cases the ambient medium was nitrogen gas at 1 atmosphere. The left side of each plot shows the density some time after the jet is "fired". The yellow portion represents the reservoir chamber, which is approximated by a very heavy gas in the simulation. As such it eventually moves, typically choking off the jet opening, but not before a well develop flow is observed. The right side shows the velocity in the vertical direction. As can be seen it is relatively straightforward to change the character of the jet by adjusting the over pressure, size of the reservoir, and specifics of the nozzle (eg compare case 1 and 2). For example, a well behaved jet is predicted for case 1, while the expansion discussed above, and seen in intial experiments (see 4.1) for the highly over-pressured case (4) is also predicted. Reducing the "puff" (case 3) results in a localized region of xenon exiting the jet. In order for the "puff" option to be viable a special arrangement would be needed because mechanical valves cannot operate on the time scale required. Although this might well be a desirable capability in future, the new jet designed and built for small over pressure work was relatively simple and effectively behaved as an infinite reservoir system (ie one that produces a long jet).

The performance of the new jet system using a simple cylindrical nozzle with an opening diameter of ~ 1mm is shown in Fig 14. The images show xenon jets propagating into nitrogen at atmospheric pressure, and ~ 1/20-1/10th an atmosphere. The vast improvement in image quality is immediately apparent compared to the images obtained in the initial experiments (section 4.1). The excellent image quality obtained at a background pressure of ~ 1atms was also a strong motivator to redesign the apparatus to allow atmospheric operation.
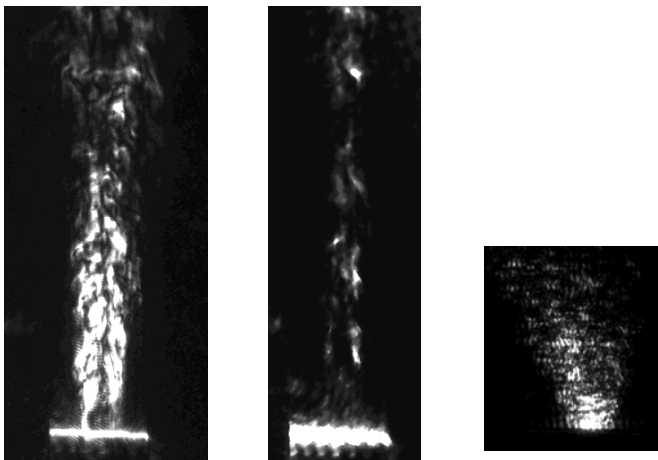
Figure 14. Shlieren images of xenon jets propagating into nitrogen: (left) at ~ 1atms; (center) ~ 1/20-1/10th atms; (right) original jet system at 1atms background pressure

5.2 Design of a mini-chamber to allow arbitrary backing pressure

From the previous experiments it is quiet clear that developing a capability to operate with higher background pressures would be highly beneficial from a diagnostics view point. In order to achieve this a new mini-chamber that would sit inside the main vacuum chamber on the Janus facility was prototyped. A thin plastic window, much like that used in a gas-filled hohlraum [27], was mounted over a small opening at one end of the chamber. The laser is focused on to this and rapidly burns through, depositing its energy inside the gas. The main chamber itself is evacuated to allow the beam to propagate to focus without breakdown occurring. This concept has strong parallels to the gas-filled hohlraum idea and there was little doubt it would work as a result. In addition, design simulations were conducted with the CALE radiation hydrocode[28]. A schematic for the Janus laser is shown in Fig. 17.
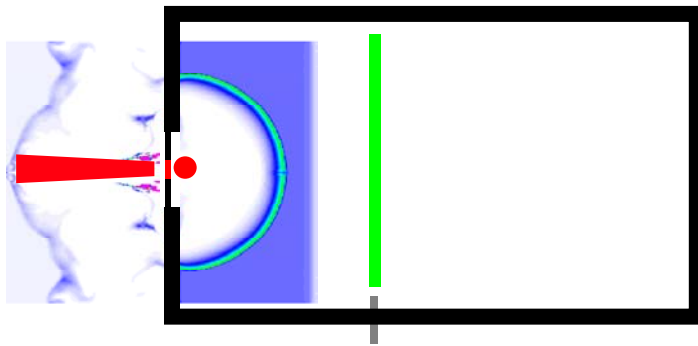
Figure 15. Schematic of a new mini-chamber for operation at the Janus laser facility. A CALE simulation (not to scale) has been superimposed showing the evolution of the blast wave, and a notional jet is depicted. The fill gas in this simulation was nitrogen at 1 atms.

The cale simulation included the window, as well as a realistic representation of the chamber wall, and laser beam. The gas in the CALE simulation was nitrogen at 1 atmosphere.

The prototype box was made from aluminum with dimensions 300 mm by 229 mm by 203 mm chosen to fit inside the Janus target vacuum chamber, and also fit an existing pair of 30 cm long glass windows thick enough (0.5 inches) to hold the pressure. On one side of the box a hole was made for a small (5 mm by 5 mm), thin (300 nm) silicon nitride film, through which the Janus main beam would propagate after having been focused down in the vacuum of the target chamber. We were able to demonstrate the feasibility of placing the air-tight box in the Janus target vacuum chamber, accurately position the box with respect to both the Janus main beam as well as a schlieren imaging system, fine-align the Janus main beam to the nitride film, and successfully capture images of blast waves with our schlieren system.

Figure 16. Blast wave propagating through p=101 kPa (1 atm) nitrogen inside the prototype box. The laser energy was E=97 J and the blastwave has propagated to a radius r=13.4 mm in a time t=4 μs. The dark,cloudy substance to the right is believed to be plasma from the silicon nitride film. The fringe pattern, as well as the two broad horizontal white streaks toward the bottom of the image are artifacts from poor quality optical windows on the box.

6. Results using the mini-chamber

The new mini-chamber design in shown in Fig 17.
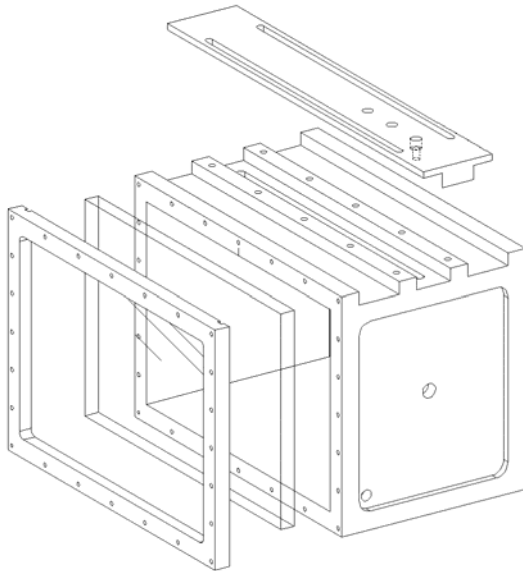
Figure 17. CAD showing an exploded view of the mini-chamber. The top plate is free to slide along the length of the box providing freedom over the location of the jet which is inserted vertically through the plate.

The nozzle for the xenon jet has an inner diameter of 1.5 mm and is inserted through the sliding top plate of the box. This effectively provided total freedom on the height of the jet opening inside the box, and on its separation from the laser

interaction region on the front plate. The separation controls the Mach number of the shock when it interacts with the jet (see section 2). In this design, the closest separation from the silicon nitride window where the blast wave originates was 10 mm. A gas system for handling the xenon gas (feeding it through the vacuum chamber, measuring the pressure, etc) was installed, now allowing us to make jets with a much smaller over-pressure (~130 kPa) compared to what was used earlier (~5.5 MPa). An example of a high quality image of a xenon jet can be seen in Fig.18.
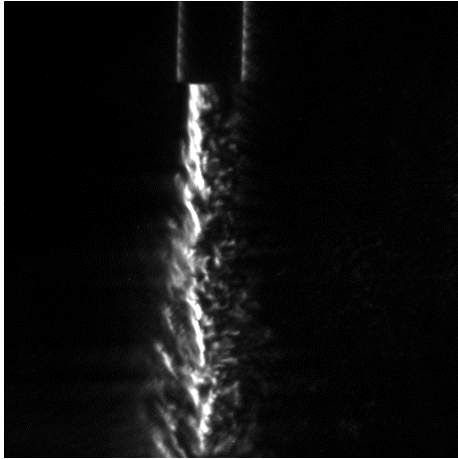
Figure 18. Xenon jet (p_{jet}=129 kPa) in background nitrogen gas (p=101 kPa) inside new box built for shock-jet interaction around 1 atm pressures. Note the regular length scale in the turbulent structures in the jet (~1.4-1.7 mm).

Special windows were made for the new box of significantly better optical quality than those used in the prototype box. The window dimension was 324 mm by 222 mm with a thickness varying across the 222 mm dimension from 11.7 mm to 12.7mm, thus creating a wedged shape that would eliminate interference patterns. To further reduce unwanted reflections, the windows were AR-coated for the wavelength (532 nm) of the Janus low energy probe beam. Overall this resulted in images of superb quality as compared to those of the prototype box (e.g., compare Figs. 12 and 13). In addition to the optical improvement the new box also allowed easy replacement of the silicon nitride film between shots from outside the box (the silicon nitride film in the prototype box had to be replaced from the inside).

We obtained images of shock-jet interaction in two different Mach number regimes, one set of images around Mach 3, and another with the jet nozzle close to the minimum distance to the box wall, resulting in Mach numbers around 7-10. The images (see Fig. 19-21) clearly show the outer limits of the expanding spherical blast wave, and just inside this one can often see what appears to be a trailing shock. These are in reality the same shock, but the schlieren imaging emphasizes structures that are perpendicular to the image plane. The "trailing" shock is where the blast wave is passing through the denser xenon jet. After the passage of the shock, what remains of the xenon jet exhibits a shortening of its characteristic length scale. Another feature visible in almost all images is debris from the silicon nitride film, which shows up as a bright cloud or bright streaks immediately to the left of the blast wave origin.
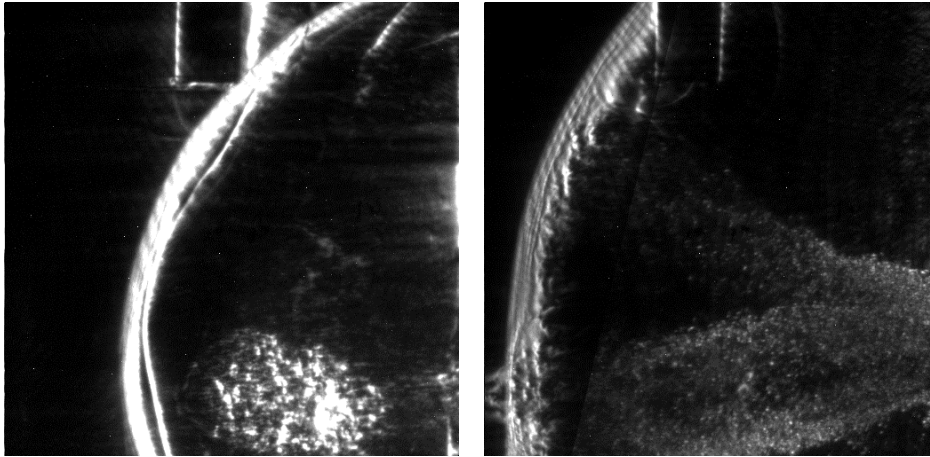
Figure 19a. (left) Blast wave in background nitrogen gas inside new box built for shock-jet interaction around 1 atm pressures (p=96 kPa). A xenon jet (p_{jet}=123 kPa) was injected through the nozzle at the top of the image. The shock speed at time of interaction is Mach 3.0. Note the apparent trailing blast wave, which is simply the part of the single blast wave that has been slowed by the xenon. The bright cloud behind the blast wave toward the bottom of the image is believed to be debris from the silicon nitride window. The image was obtained t=7 μs after the the initial laser pulse (E=87.4 J).

Figure 19b. (right) Blast wave in background nitrogen gas (p=101 kPa) interacting at Mach 2.9 with a xenon jet (p_{jet}=126 kPa) injected through the nozzle at the top of the image. The xenon can be seen as the turbulent structure immediately behind (to the right of) the expanding blast wave. The image was obtained t=20 μs after the the initial laser pulse (E=83.9 J).
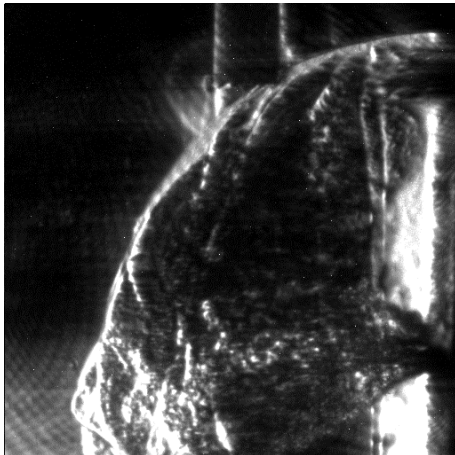
Figure 20. Blast wave in background nitrogen gas (p=99 kPa) interacting at Mach 6.5 with a xenon jet (p_{jet}=129 kPa) injected through the nozzle at the top of the image. The blast wave appears at several locations probably due to slowing down inside the xenon jet, although there may be some effect of silicon nitride debris in the left-most portion of the blast wave. The image was obtained t=6 μs after the the initial laser pulse (E=83.2 J).
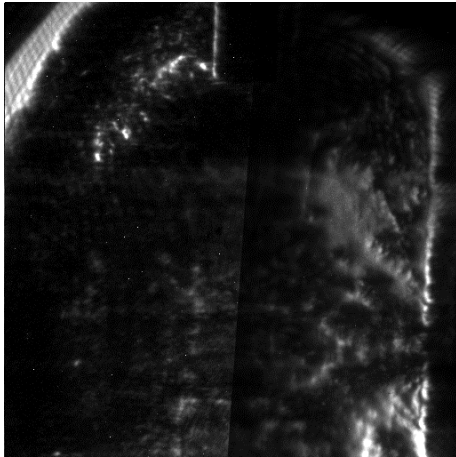
Figure 21. Blast wave (just visible in top left corner) in background nitrogen gas (p=100 kPa) interacting at Mach 10.5 with a xenon jet (p_{jet}=130 kPa) injected through the nozzle at the top of the image. The remains of the xenon jet can be seen extending from the nozzle down and to the left. Note that the characteristic length scale has been shortened (0.95 mm) compared to that of the original jet. The image was obtained t=12 μs after the initial laser pulse (E=78.8 J).

7. Discussion and design improvements to the experimental system

The results of the new experimental apparatus were obtained in 1 day of operation after a major upgrade of the Janus laser. Unfortunately, this was the only access we had to the Janus laser for the entirety of the final year of the project. This was partly because the reliability of the system took time to recover after the major upgrade, but also because demand for laser time from other programmatic user increased because of the added capability of the system. This prevented us from obtaining any further experimental results. However, the data we collected from the initial tests suggested several improvements, which were designed and implemented. These are described below.

It is particularly apparent in figure 19 that debris, which we assume to originate from the nitride window assembly is projected towards the jet interaction region which may end up compromising the experiment. To avoid interference from this debris in future experiments, we modified the box so that the gas jet nozzle is not oriented vertically, but rather pointed at an angle from the vertical, effectively raising the interaction region away from the path of the window debris. Two new sliding rails were made up, with jet nozzle angles of 30°, 45°, and 60°. For further flexibility, two new laser entrance holes (l.e.h.) were added. The original l.e.h. was located midway up one wall of the box, in the plane of the schlieren focus. One new l.e.h. was located in the same plane 33.7% of the distance from box bottom to box top, and the other new l.e.h. 75% (i.e., halfway between the original l.e.h. and the box top). The 33.7% distance was chosen so that the blast wave can propagate to as large a radius as possible before reflections from the bottom wall interfere with the experiment (as measured on a 45° cone extending from the blast wave origin, and on the good assumption that all waves propagate as $r=ct^{2/5}$, where c for the reflected wave is twice that of the original wave).

The new, tilted jet nozzles also allow another experimental configuration where the jet is not tangential to the blast wave, but rather points straight toward its origin. This configuration allows a direct measurement of the angle of the jet mixing layers as the blast wave move over the jet. This angle, usually expressed as the ratio l/L where l is the mixing layer thickness and L is the distance downstream of the nozzle, is a direct measurement of the turbulent speed $u \sim U_s(l/L)^{1/2}$ where U_s is the on-axis jet speed.

Finally, additional openings for windows were included in the base and end plate opposite the l.e.h. In future this will permit other diagnostic views, and in particular admit a laser sheet diagnostic, which has also been designed based on using the existing probe laser and cylindrical optics. The advantage of a sheet diagnostic is that is samples a narrow spatial region, and is also the basis of other, more powerful optical diagnostics.

8. Exit Strategy

The original intention was for the work if successful would transition into the High Energy Density Experimental Program. At the closing of funding, progress was judged to be sufficiently promising that at least one further test experiment in FY05 would be carried out under this program.

Acknowledgements

References

1) Lord Rayleigh, Scientific Papers II (Cambridge University Press, Cambridge, 1900), p 200.; G I Taylor, Proc. Royal Soc. **A201**, 159, (1950)
2) G Dimonte et al, Phys Fluids **16**(3), 1668 (2004)
3) Y Andreopoulos, J Agui, and G Briassulis, Ann. Rev. Fluid Mech. **32**, 309 (2000)
4) A Hokan and J Andreopoulos, Phys fluids **A4**(11) 2562, (1992)
5) L Hasselink and B Sturtevant, JFM **196**, 513 (1988)
6) F Poggi, M Thoremby and G Rodriguez, Phys Fluids **10**(11), 2698 (1998); F. Poggi et al, in Proceedings of the sixth workshop on the Physics of Compressible Turbulent Mixing Marseille France, (1997)
7) A N Aleshin, S G Zaitsev and E V Lazareva, Rus. J. Comp. Mech **1**(2), 33 (1993)
8) S Lee, S Lele, and P Moin, JFM **340**, 225 (1997)
9) P Vorobief et al, Phys. Rev. E **68**, 065301(R)(2003)
10) S Zhang et al, Phys Fluids **16**(5),1203 (2004)
11) J W Jacobs and C E Niederhuas, in Proceedings of the sixth workshop on the Physics of Compressible Turbulent Mixing Marseille France, (1997)
12) J Edwards et al, Phys. Plas **7**(5) 2099 (2000)
13) J F Foster et al, Phys Plasmas **9**(5), 2251 (2002)
14) S G Glendinning et al, Phys. Plas. **10**(5), 1931 (2003)
15) B Blue et al, accepted for publication in PRL (2004)
16) G S Settles, "Schlieren and Shadowgraph Techniques", Springer-Verlag, New York 2001
17) J Grun et al, PRL **66**, 2738, (1991)
18) A D Edens et al, Phys. Plas **11**(11), 4968 (2004)
19) R L Kauffman, LLNL Annual report, UCRL-50021-85 (1986)
20) R Kodama et al, J. Appl. Phys. **59**, 3050 (1986)
21) L I Sedov, Similarity and Dimensional Methods in Mechanics, Academic Press 1997 (New York)
22) P E Dimotakis, JFM **409**, 69 (2000)
23) J Edwards et al, PRL 87, 8708 (2001)
24) J F Hansen, submitted to PRL UCRL-JRNL-205848
25) P A Thompson, Compressible Fluid Dynamics (Advanced engineering series, 1988)
26) L. H Howell and J A Greenough, J. Comp. Phys. **184**, 53 (2003)
27) J D Lindl et al, Phys Plasmas **11**(2), 339 (2004)
28) R T Barton, Numerical Astrophysics (Jones and Bartlett, Boston, 1985)

APPENDIX 1

Laser shot time

<u>FY02</u>
2+2=4 weeks of laser time
- Implemented diagnostics (schlieren, interferometer, spectrometer).
- Characterized blast waves originating at laser focus on pin or foil.
- Examined nature of radiative shocks in xenon.
- Tried interaction between blast wave (N_2) and high over-pressure jet (N_2).

<u>FY03</u>
3+3+1=7 weeks of laser time
- Implemented new experimental configuration that allowed two simultaneous blast waves.
- Examined interaction between two blast waves.
- Examined interaction between blast wave (N_2) and low density solid (aerogel).
- Repeated characterization of blast waves using target pins of low-Z and high-Z materials (graphite and tungsten).
- Implemented a low over-pressure jet.
- Established optimum background gas pressure for best visibility of jet.
- Examined interaction between blast wave and jet on laser side of pin vs. "shadow" side of pin.
- Examined interaction between blast wave (N_2) and low over-pressure jet (N_2 and Xe).
- Experimented with nozzle shapes for best jet structure.
- Improved schlieren system (knife edge block vs. pin block).
- Characterized blast waves in Xe/N_2 mixtures in order to confirm theoretical model for radiative shocks.
- Demonstrated creating blast waves in atmospheric pressure using prototype box.

<u>FY04</u>
2 weeks of laser time*
- Examined interaction between blast wave (N_2) and low over-pressure jet (Xe) inside new atmospheric pressure box.

* Problems with the Janus laser after a facility upgrade reduced our effective shot time to one day (one afternoon + following morning).

Laboratory observation of secondary shock formation ahead of a strongly radiative blast wave

J.F. Hansen, M.J. Edwards, D. Froula, and G. Gregori

Lawrence Livermore National Laboratory, Livermore, CA 94550, USA

A. Edens and T. Ditmire

University of Texas at Austin, Austin, TX 78712, USA

Abstract

High Mach number blast waves were created by focusing a laser pulse on a solid pin, surrounded by nitrogen or xenon gas. In xenon, the initial shock is strongly radiative, sending out a supersonic radiative heat wave far ahead of itself. The shock propagates into the heated gas, diminishing in strength as it goes. The radiative heat wave begins to stall, causing a second shock to form. The second shock continues to propagate long after the initial shock can no longer be observed. This second shock is a new phenomena that has not previously been discussed in literature. Numerical simulation clarifies the origin of the second shock, and its position is consistent with an analytical estimate.

Interstellar space consists of a tenuous plasma capable of propagating shocks over great distances. Shocks originate in supernova (SN) explosions [1–5] and other astrophysical phenomena (e.g., T Tauri stars [6] and stellar winds [7]) and are important to understand as they mix up interstellar matter and thus affect mass-loading, stellar formation [8–10] and the history of the Milky Way and other galaxies. The shocks have high Mach numbers and can be strongly radiative [11]. Until recently, these properties have not been easily attainable in laboratories, but using high-power lasers, similar shocks can be now created and studied experimentally [4, 12–18]. We have conducted experiments at the Janus laser at the Lawrence Livermore National Laboratory in California, comparing the shock expansion for non-radiative and radiative shocks, and we report here on our findings, including a new phenomena that has not previously been observed.

A SN shock expanding through interstellar space sweeps up interstellar material, most of which ends up in a shell just behind the shock. Once the shock has swept up more mass than what was initially present, the shock could be regarded as without characteristic length or time scales, and so one would expect the well-known self-similar motion of a Taylor-Sedov blast wave [19–22], $r_s \propto t^\alpha$, where r_s is shock radius, t is time, and the exponent $\alpha = \frac{2}{5}$. This assumes that there are no density gradients in the swept region of space and that energy is not radiated from the shock. If radiation removes energy from the shock in an optically thin environment, analytical and numerical studies predict a slower shock expansion, such as $\alpha = \frac{2}{7}$ ("pressure-driven snowplow"), $\alpha = \frac{1}{4}$ ("momentum-driven snowplow"; the shock is simply coasting) [11, 23], and $\frac{2}{7} < \alpha < \frac{2}{5}$ (thermal energy of the shocked gas is not completely radiated away) [22, 24]. If the environment is not optically thin, radiation is reabsorbed in the upstream material and if the shock is travelling fast enough a supersonic, radiative heat wave (RHW) breaks away from the shock in a situation analogous to a supercritical shock wave [21]. It has been shown that the shock and RHW will coexist and in the self-similar limit propagate as $r \propto t^\alpha$ where α is larger for the shock [25]. This means that the shock will eventually catch RHW, after which a second self-similar state is obtained in which RHW is of the adiabatic type and the shock moves in a classical Taylor-Sedov trajectory with $\alpha = \frac{2}{5}$. In this manuscript we report on the additional possibility that prior to the shock catching RHW, the latter enters a transonic regime where it generates a second shock.

We create spherically expanding blast waves in the following fashion: a high-power infrared pulsed laser (1064 nm wavelength) is focused onto the tip of a solid (stainless steel)

pin surrounded by an ambient gas (nitrogen or xenon) typically at a pressure of about 1 kPa (density $\sim 10^{-5}$ g / cm^3). The laser pulse (5 ns duration and energy ranging from 1 J to 150 J) ablates the pin and rapid expansion of ablated material shocks the ambient gas. The initial shock travels radially outward from the pin; most of the shocked gas is concentrated in a shell immediately behind the shock front (the blast wave consists of shock and shell). The blast wave velocity drops as more and more of the ambient gas is accumulated and set in motion by the passing shock. When the mass of swept up material is much larger than the initially ablated material, the motion of the blast wave becomes self-similar. We can conservatively estimate the radius at which this happens, assuming that all laser energy is deposited in pin material, heating it uniformly. (Loss of laser energy, e.g., due to misalignment between the laser beam and the pin, and non-uniform heating will lower our estimated radius.) For example, a 150 J laser pulse (the highest energy used in our experiments) ablates an amount of iron such that when the blast wave has traveled 1.8 mm, it will have swept up a much larger (ten times larger) nitrogen mass. If the laser energy is 10 J and the ambient gas is xenon, the corresponding distance is 0.4 mm.

We obtain image and spectrometer data of the shocks to deduce blast wave radius as a function of time and temperature profiles across the shock. To image a blast wave on spatial scales up to ≈ 5 cm, we use two lenses in a telescope configuration and a gated, single-frame, high-speed CCD camera (2 ns gate), along with a low energy, green laser pulse ($\lambda = 532$ nm wavelength, 15 ns duration) as a backlighter. Blast wave radius as a function of time is obtained by employing a schlieren technique so that only laser light perturbed by the plasma is imaged; light which has not been deflected is removed at the telescope focal point by a small ($\approx 500 \,\mu$m) beam block. With this method, image brightness corresponds to the spatial derivative of plasma electron density, and the blast wave structure is readily seen. Schlieren images were obtained from 5 ns up to 35 μs after the initial, ablative laser pulse. A spectrometer was used to obtain spectral line intensity as a function of position (ahead of and behind the blast wave), which was then Abel inverted to get spectral line intensity as a function of radius. Temperature as a function of radius was then calculated from pair-wise line ratios.

Examples of images using nitrogen as the ambient gas can be seen in Fig. 1. In each image, the laser ablating the target pin is incident from the left. The pin is clearly visible, as is the expanding blast wave. [Note that the shock is not exactly centered on the pin and

rod composite.jpg
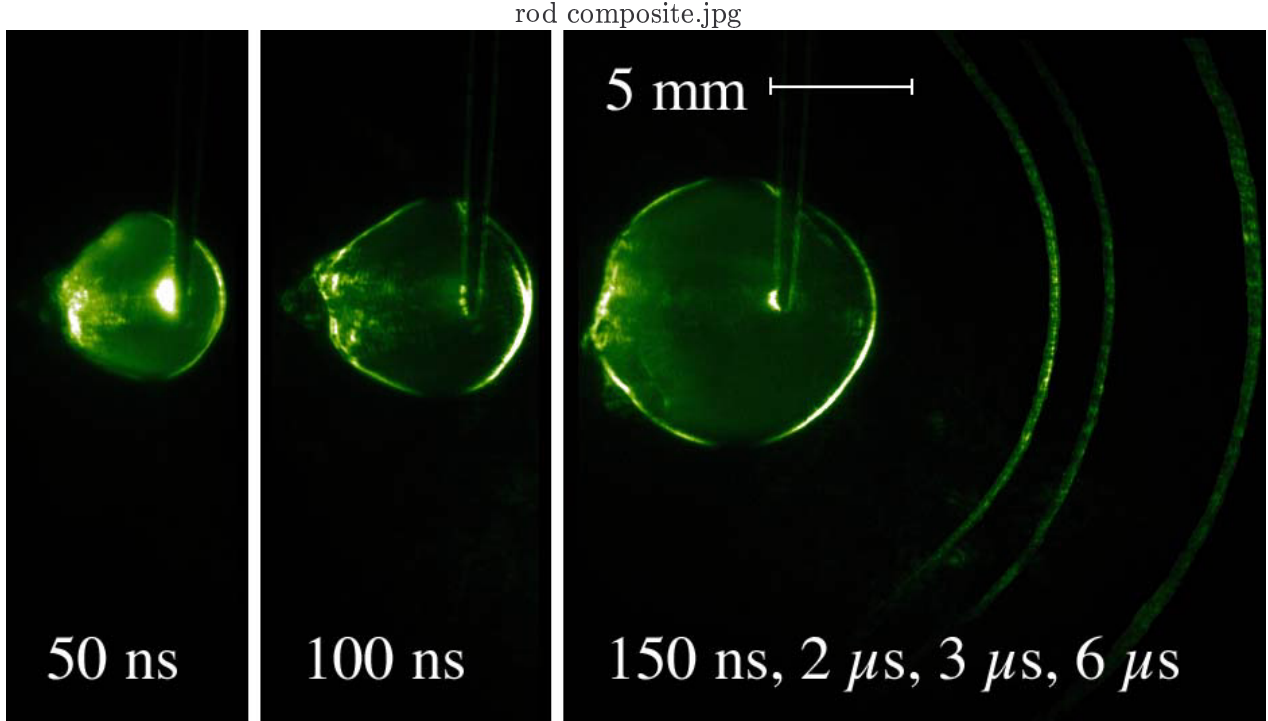
FIG. 1: Blast wave expansion through ambient nitrogen gas (1.3 kPa) at times $t = 150$ ns to $6\,\mu$s after an ablative laser pulse (energy $E = 10$ J, duration 5 ns) is focused on a solid pin (visible in images, pointed down). The laser pulse was incident from the left. The shock is spherical (except on the laser side due to laser-plasma interaction) and its growth is consistent with a Taylor-Sedov blast wave. The image to the right ($t = 150$ ns to $6\,\mu$s) is a composite of four images (with overlapping pin locations).

also is not perfectly spherical; deviation from sphericity is evident on the laser side of the pin. A 2D computer simulation (computed by the CALE code [26], an arbitrary Lagrangian-Eulerian code including both hydrodynamic and radiative effects) shows how laser-plasma interaction causes pre-ionization and preheating of the plasma on the laser side. The shock then propagates through a non-uniform plasma, leading to a non-uniform shock expansion. This effect is further discussed by Edens *et al.* [27].] The shock expansion settles (to within measurement error) into the Taylor-Sedov relationship for a blast wave $r_s \propto t^{2/5}$ after an initial, brief, non-self similar phase. This was expected for a shock where the radiative effects are minimal. (It also appeared that $r_s \propto (E/\rho_0)^{1/5}$, where E is the laser energy and ρ_0 is the density of the ambient gas, also consistent with a Taylor-Sedov blast wave.)
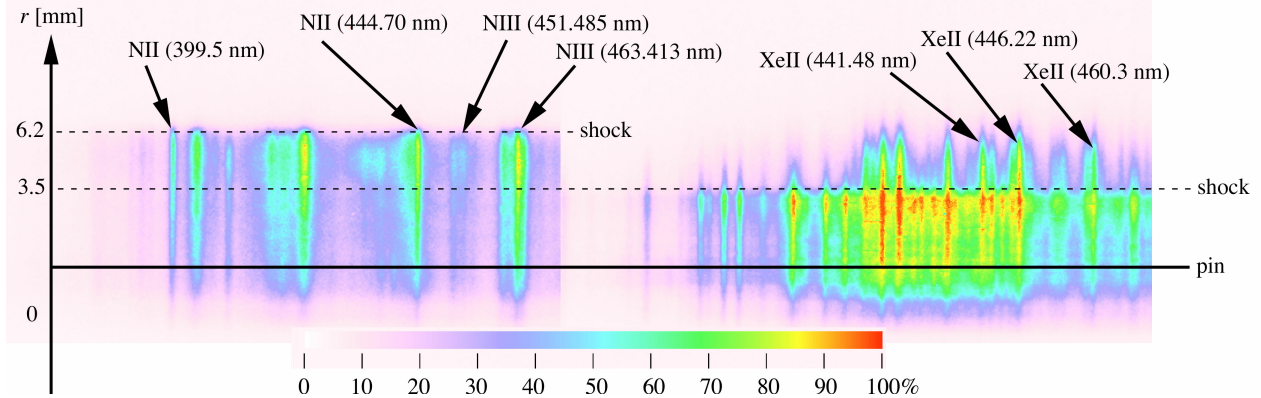
FIG. 2: Spectra for nitrogen (left) and xenon (right) at $t = 150\,\text{ns}$. The location of the pin is marked with a solid line. The shock locations, as obtained from schlieren images, are indicated by dashed lines at radii $r = 6.2\,\text{mm}$ for nitrogen and $r = 3.5\,\text{mm}$ for xenon.

Emission spectroscopy data in the near ultraviolet range was readily obtained at and behind the blast wave in nitrogen, but no readings discernible from noise were possible ahead of the shock. Two temperature distributions calculated from pair-wise line ratios of two NII lines (399.5 nm and 444.70 nm) and two NIII lines (451.485 nm and 463.413 nm) generally agreed with each other except for a constant offset of $\sim 1-2\,\text{eV}$ (presumably from measurement error and from non-LTE effects). Figure 2 shows an example spectra taken at a time $t = 150\,\text{ns}$ after the initial laser pulse ($E = 10\,\text{J}$), with electron temperatures in the range $4\,\text{eV}$ to $7\,\text{eV}$ at and behind the shock. We see no signs of pre-heated gas ahead of the shock, suggesting that radiative effects are minimal.

Examples of images using xenon as the ambient gas can be seen in Fig. 3. With its higher atomic number, xenon radiates more strongly than nitrogen, and there are several notable differences in the images pointing to radiative effects: (a) plasma emission from pre-heated gas, that is gas heated by the radiation from the shock, is clearly visible as a glow surrounding the shock at early times ($t \lesssim 400\,\text{ns}$). (b) The shock expansion is slower than in nitrogen, even when accounting for the $r_s \propto \rho^{-1/5}$ factor from the higher density of xenon. (c) The shock weakens ($t \approx 1\,\mu\text{s}$ to $4\,\mu\text{s}$) and gets increasingly difficult to detect (d) Before the initial shock becomes undetectable ($t \approx 8\,\mu\text{s}$), a second shock forms out ahead of the initial shock. This second shock is a phenomena that has not previously been discussed in literature in this context. It is not surrounded by a glow of pre-heated gas, and it continues
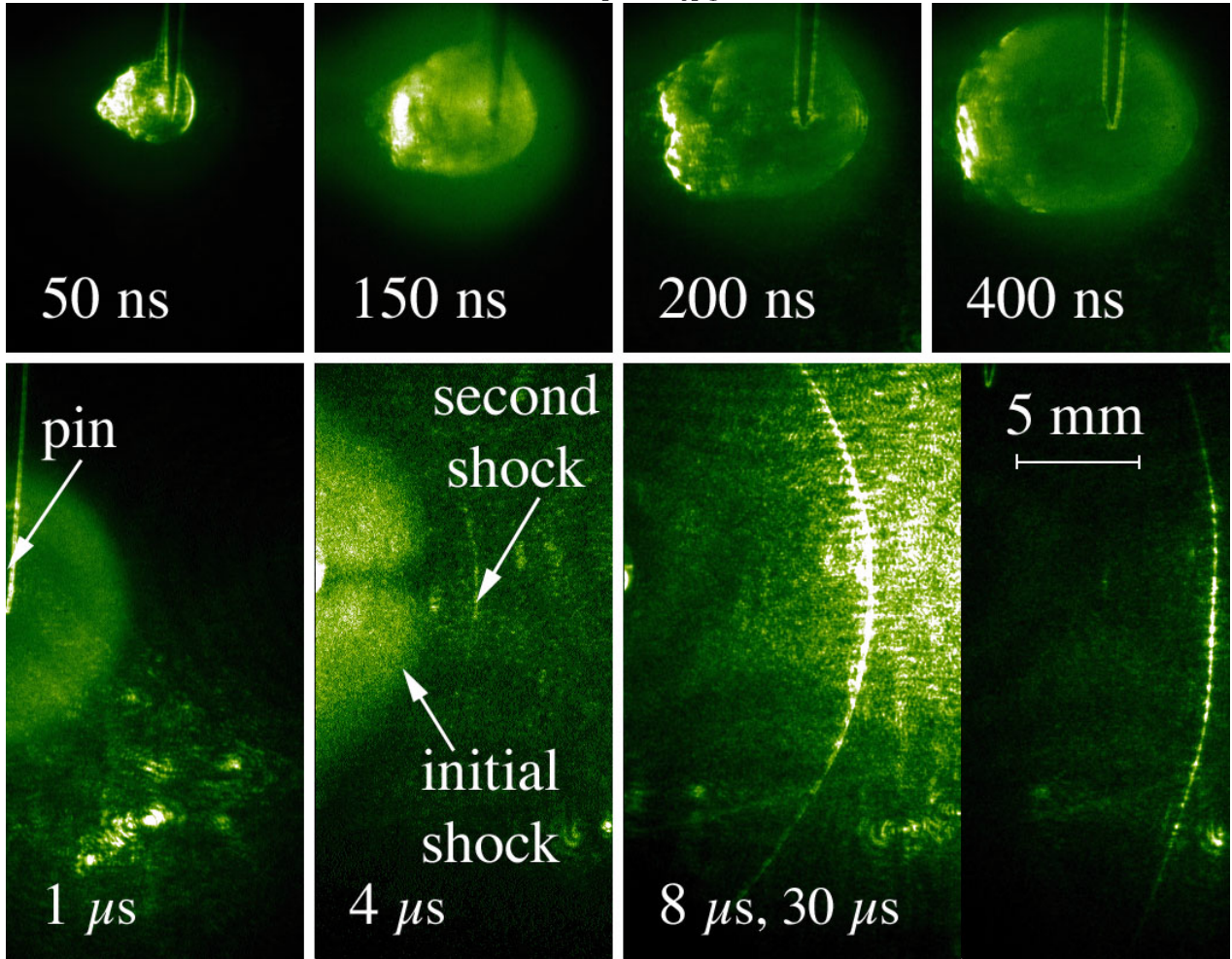
FIG. 3: Blast wave expansion through ambient Xe gas (1.3 kPa) at times $t = 50$ ns to $30\,\mu$s after an ablative laser pulse (energy $E = 10$ J, duration 5 ns) is focused on a solid pin (visible in images, pointed down; pin location in bottom row of images is at the left edge of each image). The laser pulse was incident from the left. The initial shock is strongly radiative (super-critical) and preheats the ambient gas. At $t = 150$ ns both the initial shock and the preheated gas ahead of it are clearly visible. At $t \approx 1\,\mu$s the initial shock begins to dissipate, and the shock front is no longer obviously sharp. At $t \approx 4\,\mu$s a second shock appears (located at tip of arrow), ahead of the initial shock. The second shock continues to expand while the initial shock gradually becomes undetectable. The final image ($t = 8\,\mu$s, $30\,\mu$s) is a composite of two images (with overlapping pin locations).

to propagate long after the initial shock can no longer be detected.

Spectroscopy data (see Fig. 2) confirm that the temperature immediately ahead of the initial shock is roughly the same as behind it. A few millimeters in front of the shock the temperature then drops sharply (to noise levels). For example, at $t = 150\,\text{ns}$ and a laser energy of $E = 10\,\text{J}$ (see Fig. 2), the temperatures in the xenon case were in the range $1.6\,\text{eV}$ to $3.6\,\text{eV}$, calculated from pair-wise line ratios of three XeII lines, 441.48 nm, 446.22 nm, and 460.3 nm. From measured temperatures, radii, and velocities, and a deduced (using a screened hydrogenic model [28]) average ionization of 5.6, we calculate that the initial energy is distributed so that 52%-90% is in the preheated gas, 8%-22% is heat and internal energy in and behind the shock, and 4%-31% is kinetic energy; errors depend on uncertainties in temperature and locating the exact boundary of the preheated gas.

We measured the initial shock radius in 63 laser shots (with ten different combinations of laser energy and xenon pressure) and found $r_s \propto t^{0.470 \pm 0.126}$. While uncertainty in the time exponent is relatively large, it is small enough to rule out both the 2/7 and the 1/4 power law dependences. In 39 shots (with six different combinations of laser energy and xenon pressure) the second shock radius was found to be $r_s \propto t^{0.486 \pm 0.083}$. Figure 4 shows an example of radius vs time data.

To help interpret our experimental results we ran a 1D numerical simulation using the LASNEX code [29] which captures the observed sequence of events rather well. The simulation follows the discussion of this process given by Reinicke and Meyer-ter-Vehn [25], and also includes the new result, the birth of a second shock ahead of the initial shock. [We also performed additional calculations with modified initial conditions to confirm the origin of the second shock (described below) and calculations which excluded radiative effects. In the latter case the deposited energy was reduced (to ~20%) in order to match the shock trajectory/velocity of the full calculation (shock radius versus time from the full calculation is plotted for comparison in Fig. 4 above).] At the end of the laser pulse ($t = 5\,\text{ns}$), motion is still strongly influenced by the details of the initial conditions. The initial shock (which we will refer to as S1) is traveling in excess of $60\,\text{km / s}$ and is strongly radiative (supercritical), driving a highly supersonic radiative heat wave (which we will refer to as RHW) far out ahead of itself (RHW radius $r_h \approx 2.5\,\text{mm}$). The S1 compression η is very high ($\eta > 20$), a feature consistent with strongly radiating shocks. By $t \approx 20\,\text{ns}$, memory of the details of the initial conditions is no longer apparent. S1 has expanded to $r_s \approx 1.4\,\text{mm}$ and slowed
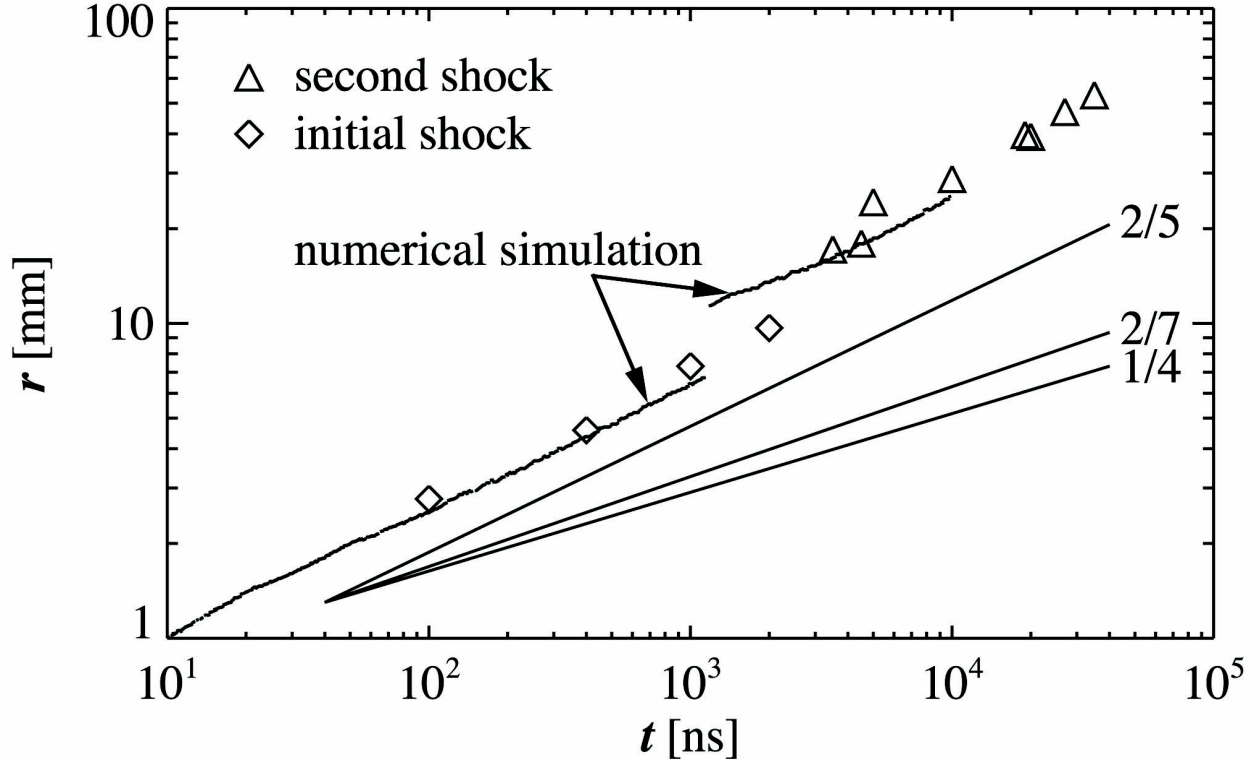
FIG. 4: Plot of shock radius as a function of time as measured in the experiment, compared to a numerical simulation and to analytical estimates of shock propagation. The 1D numerical simulation by the LASNEX code shows the largest radius at which the compression $1/\eta > 1.25$. The analytical estimates are represented by the three (displaced) lines with slopes $\alpha = \frac{2}{5}$, $\frac{2}{7}$, and $\frac{1}{4}$. (Error bars for radius and time in this plot would be smaller than the plot symbols. There is a 28% rms fluctuation in laser energy.)

to $\sim 30\,\mathrm{km/s}$, but is still strongly radiative. Only about one eighth of the total energy now resides inside S1 with the remainder in RHW which extends to $r_h \approx 4\,\mathrm{mm}$. The energy loss rate can be quantified [24] by the parameter $\varepsilon = -\frac{\mathrm{d}E}{\mathrm{d}t}\left(2\pi\rho_0\right)^{-1}r_s^{-2}\left(\frac{\mathrm{d}r_s}{\mathrm{d}t}\right)^{-3}$, where E is the total energy content of S1. (In a fully radiative case, in which radiation escapes to infinity, the incoming kinetic energy swept up by a shock is entirely radiated away and the shocked material collapses to a thin shell directly behind the shock. The denominator is then precisely the rate at which kinetic energy is accumulated, and $\varepsilon = 1$. For an adiabatic case, $\varepsilon = 0$.) In our case, the simulation has $\varepsilon \approx 0.8$ at $t = 20\,\mathrm{ns}$, consistent with a strongly radiative shock, and is gradually decreasing. [We note that for $\varepsilon < 0.8$ Liang and

Keilty [22] calculates a shock expansion exponent $\alpha > 0.34$ (for any reasonable value of the adiabatic index γ) which is consistent with our observed expansion $\alpha = 0.470 \pm 0.126$.] By $t = 100 \, \text{ns}$, S1 has advanced to $r_s \approx 2.5 \, \text{mm}$ and is moving at ˜$10 \, \text{km/s}$. RHW is located at $r_h \approx 7 \, \text{mm}$ and is slowing rapidly (see Fig. 5). The fraction of the total energy inside S1 has fallen below one tenth. Although S1 is still calculated to be supercritical, the rate at which S1 is accumulating energy as it sweeps up hot gas (preheated by RHW) begins to balance the radiative loss rate ($\varepsilon \approx 0$). The S1 compression is now only $\eta \approx 6$, which is nearly the same ($\eta \approx 7$) as we calculate for a shock traveling at this velocity in xenon when excluding radiative effects. From $t \approx 150 \, \text{ns}$, S1 enters a transitional phase. It is still traveling fast enough to be supercritical, but the energy inside S1 is now slowly increasing as the accumulated energy exceeds the radiative loss rate ($\varepsilon < 0$). For comparison with the estimate from the experimental data, we calculate an electron temperature of $3.4 \, \text{eV}$ at this time, and the energy is distributed so that 85% is in RHW, 12% is heat in and behind S1, and 4% is kinetic energy. By $t = 300 \, \text{ns}$, S1 has expanded to $r_s \approx 4 \, \text{mm}$ and its velocity has fallen to ˜$6 \, \text{km/s}$, or twice the speed of sound in the RHW plasma into which S1 propagates. We calculate that such a shock would no longer be fast enough in xenon to be supercritical. The S1 compression is barely above $\eta \approx 2$. (For comparison, in a calculation where the radiative effects are excluded, but the shock velocity is matched, the compression is still $\eta \approx 7$.) The low compression and $\varepsilon < 0$ should both lead to a shock expansion exponent slightly in excess of 2/5, but unfortunately the experimental error bars are much too large to distinguish these subtleties. S1 continues to weaken as it expands. The RHW itself has only moved ˜$2 \, \text{mm}$ during the last $200 \, \text{ns}$ ($r_h \approx 9 \, \text{mm}$) and its velocity has dropped to be comparable to that of S1. From here on S1 gradually makes ground on the stalling RHW, but before S1 can catch RHW the latter enters the transonic regime (relative to the sound speed in the hot plasma behind RHW) and begins to drive a non-linear disturbance which eventually ($t \approx 1.2 \, \mu\text{s}$) breaks into a shock (which we will refer to as S2). At this time RHW drops behind S2.

Because the formation of S2 is a new result we have gone to some effort to ensure that our interpretation is correct. Most importantly we collected a large amount of experimental data around the transition time (˜$1 \, \mu\text{s}$). This data is essentially the same as that shown in Fig. 4 but with much finer time resolution. It categorically shows S1 and S2 simultaneously and follows their evolution. We will expand upon this at a later date. We also performed
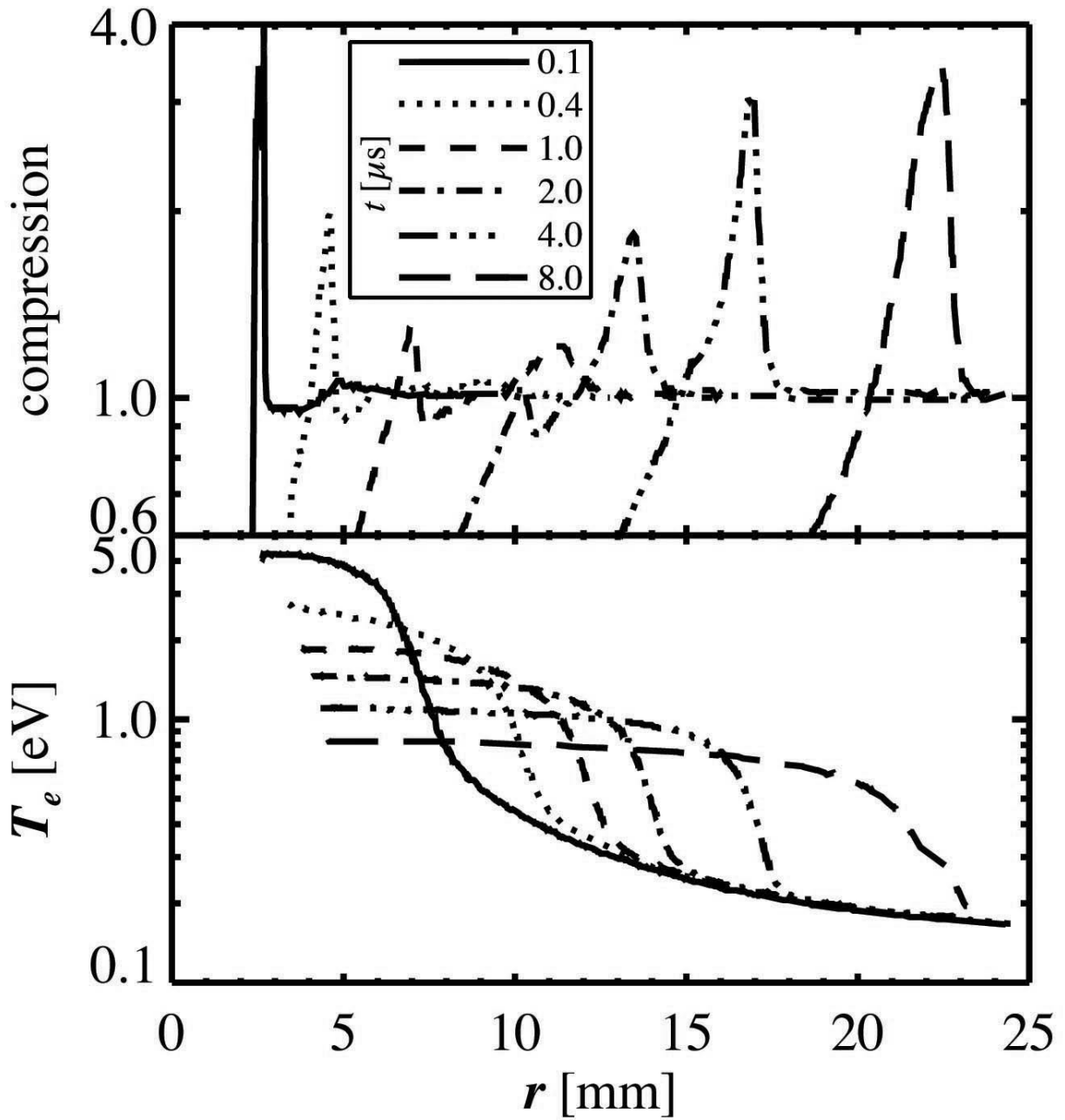
FIG. 5: Numerical simulation showing compression η (upper graph) and electron temperature (lower graph) as a function of radius for six different times. At $t = 100\,\text{ns}$ the initial shock has $\eta \approx 6$. Note the initial shock dissipating and the second shock being born at the radiative heat wave front.

two confirmatory LASNEX calculations. In the first we took the RHW temperature distribution well before the formation of S2 and imposed it in a stationary, uniform xenon gas. As expected, RHW advanced and S2 formed just as in the full calculation. In the second calculation, we used a spherical piston to drive a shock with the same trajectory as in the full calculation. This produced nearly identical results to the full calculation, demonstrating that the observed dynamics result from the radiative nature of S1, and are not substantially influenced by the nature of the driving source. This was also confirmed experimentally by a limited set of shots on graphite pins, which yielded the same results. Finally, we compared the observed formation location of S2 to the following simple, analytical estimate for where S2 forms:

Consider the simple 1D fluid equations for conservation of mass $\rho_1 u_1 = \rho_2 u_2$ and momentum $p_1 + \rho_1 u_1^2 = p_2 + \rho_2 u_2^2$ in the lab frame of RHW, where subscript 1 denotes the region ahead of RHW, and subscript 2 denotes the region behind RHW. Assuming an ideal gas (so that $p = \rho c^2$ where c is the speed of sound) we combine these to obtain

$$\frac{\rho_2}{\rho_1} = \frac{c_1^2 + u_1^2 \pm \sqrt{\left(c_1^2 + u_1^2\right)^2 - 4c_2^2 u_1^2}}{2c_2^2}. \tag{1}$$

A supersonic $(u_1 > c_1)$ RHW and a real compression $\eta \equiv \rho_2/\rho_1$ requires $u_1 \geq c_2 + \sqrt{c_2^2 - c_1^2} \approx 2c_2$ (where the approximation is valid because the temperature behind RHW is much higher than the temperature before it), i.e., requires the mixed Mach number $M \equiv u_1/c_2 \geq 2$. Once the Mach number drops to 2, RHW can no longer fulfill Eq. 1, and a shock (S2) forms at RHW (analogous to when a blast wave forms ahead of a fireball) [21, 30, 31]. S2 immediately moves ahead of RHW and acts to slow down u_1 so that RHW is now subsonic (satisfying $u_1 \leq c_2 - \sqrt{c_2^2 - c_1^2} \approx c_1^2/2c_2$). To estimate when RHW slows to Mach 2 and what its radius r_h then is, we can use Barenblatt's solution for an instantaneous point release of energy [25, 32]. (This is a reasonable estimate [25] because most of the energy that S1 can lose through radiation is lost at an early stage when there is a large separation between S1 and RHW.) Assuming that we can write the radiative conductivity of the ambient gas as $\chi = \chi_0 \rho^a T^b$, then Barenblatt's solution gives:

$$T(r,t) = \frac{m_0}{R}\left(1 - \left(\frac{r}{r_0}t^\delta\right)^2\right)^{\frac{1}{b}}\frac{\tau_0}{t^{3\delta}} \tag{2}$$

and

$$r_h(t) = r_0 t^\delta \tag{3}$$

where m_0 is the molecular weight, R is the ideal gas constant, $\delta = 1/\left(3b + 2\right)$, $r_0 = \left(K_1^b K_2\right)^\delta$, and $\tau_0 = \left(K_1^2 K_2^{-3}\right)^\delta$, where

$$K_1 = \frac{\gamma - 1}{2\pi B\left(\frac{3}{2}, 1 + \frac{1}{b}\right)} \frac{E}{\rho_0} \tag{4}$$

and

$$K_2 = \frac{2\chi_0\left(\gamma - 1\right)}{\left(\frac{R}{m_0}\right)^{b+1} \rho_0^{1-a}} \frac{1}{b\delta} \tag{5}$$

where $B\left(x, y\right)$ is the beta function. Using values for our experiment in xenon, $E = 10\,\mathrm{J}$, $\rho_0 = 78\,\mathrm{g/m^3}$, $\gamma = 1.2$, and $\chi = 10^{-44}\rho^{-2.2}T^{10}$ in SI-units, we find that the RHW Mach number $M\left(r_h, t\right) = \frac{\mathrm{d}r_h(t)}{\mathrm{d}t}\sqrt{\frac{m_0}{RT(r_h,t)}}$ drops to Mach 2 when $r_h \approx 10\,\mathrm{mm}$. In the experiment we first observed S2 with $r_h \approx 12\,\mathrm{mm}$, in reasonable agreement with the analytical estimate, particularly considering that S2 must grow some before becoming observable (the schlieren technique is not infinitely sensitive).

From all the above, we summarize the blast wave evolution in xenon in the following steps: (1) The laser energy is deposited in pin material which then becomes very hot. (2) The heated pin material expands rapidly, pushing at the surrounding gas, setting up a strong, radiative S1. (3) Radiation from S1 heats the surrounding gas. The flux is high enough that S1 is supercritical [21], driving a supersonic RHW that travels rapidly outward, leaving a large separation between S1 and RHW. [Note that RHW is only obtained when the surrounding gas is optically thick, so that the radiated energy is deposited in the surrounding gas, heating it up; if the surrounding gas is optically thin, the energy is lost (transported to "infinity").] (4) S1 sweeps up enough material that the details of its initial conditions become unimportant. (5) S1 slows and its ability to radiate efficiently quickly decreases. The energy loss rate $\varepsilon < 0.8$. (6) S1 is traveling into the counter pressure of hot RHW plasma, which is becoming comparable to the ram pressure, i.e., S1 can no longer be considered strong and has a much lower compression than if there had been no preheating. This is just like the point explosion with counter pressure discussed by Zel'dovich and Raizer [21]; the Mach number drops rapidly, and the post-shock compression reduces correspondingly. (7) RHW stalls and creates S2. This is precisely analogous to the shock break out from the fireball of a nuclear explosion [21]. The transition occurs when the Mach number of RHW reaches ~ 2 [30, 31]. (8) S1 continues to weaken until it dissipates (or until S1 breaks through RHW, as discussed by Reinicke and Meyer-ter-Vehn [25]). (9) S2 is essentially non-radiative and once it has swept up enough mass (doubled its initial radius), it propagates like $r_s \propto t^{2/5}$,

provided it remains strong.

We thank Dwight Price and the staff at the Janus facility for their valuable assistance.

---

[1] E. Müller, B. Fryxell, and D. Arnett, Astron. Astrophys. **251**, 505 (1991).

[2] J. I. Reed, J. J. Hester, A. C. Fabian, and P. F. Winkler, Astrophys. J. **440**, 706 (1995).

[3] G. Sonneborn, C. S. J. Pun, R. A. Kimble, T. R. Gull, P. Lundqvist, R. McCray, P. Plait, A. Boggess, C. W. Bowers, A. C. Danks, et al., Astrophys. J. Lett. **492**, L139 (1998).

[4] B. A. Remington, D. Arnett, R. P. Drake, and H. Takabe, Science **284**, 1488 (1999).

[5] N. Bartel, M. F. Bietenholz, M. P. Rupen, A. J. Beasley, D. A. Graham, V. I. Altunin, T. Venturi, G. Umana, W. H. Cannon, and J. E. Conway, Science **287**, 112 (2000).

[6] B. Reipurth and G. Sandell, Astron. Astrophys. **150**, 307 (1985).

[7] J. R. Jokipii, C. P. Scott, and M. S. Giampapa, eds., Cosmic Winds and the Heliosphere (University of Arizona Press, 1997).

[8] C. F. McKee and B. T. Draine, Science **252**, 397 (1991).

[9] D. A. Allen and M. G. Burton, Nature **363**, 54 (1993).

[10] R. I. Klein and D. T. Woods, Astrophys. J. **497**, 777 (1998).

[11] J. M. Blondin, E. B. Wright, K. J. Borkowski, and S. P. Reynolds, Astrophys. J. **500**, 342 (1998).

[12] J. C. Bozier, G. Thiell, J. P. LeBreton, S. Azra, M. Decroisette, and D. Schirmann, Phys. Rev. Lett. **57**, 1304 (1986).

[13] J. Grun, J. Stamper, C. Manka, J. Resnick, R. Burris, J. Crawford, and B. H. Ripin, Phys. Rev. Lett. **66**, 2738 (1991).

[14] D. Ryutov, R. P. Drake, J. Kane, E. Liang, B. A. Remington, and W. M. Wood-Vasey, Astrophys. J. **518**, 821 (1999).

[15] K. Shigemori, T. Ditmire, B. A. Remington, V. Yanovksy, D. Ryutov, K. G. Estabrook, M. J. Edwards, A. J. MacKinnon, A. M. Rubenchik, K. A. Keilty, et al., Astrophys. J. **533**, 159 (2000).

[16] H. F. Robey, J. O. Kane, B. A. Remington, R. P. Drake, O. A. Hurricane, H. Louis, R. J. Wallace, J. Knauer, P. Keiter, D. Arnett, et al., Phys. of Plasmas **8**, 2446 (2001).

[17] P. A. Keiter, R. P. Drake, T. S. Perry, H. F. Robey, B. A. Remington, C. A. Iglesias, R. J. Wallace, and J. Knauer, Phys. Rev. Lett. **89**, 165003 (2002).

[18] S. Bouquet, C. Stehle, M. Koenig, J.-P. Chieze, A. Benuzzi-Mounaix, D. Batani, S. Leygnac, X. Fleury, H. Merdji, C. Michaut, et al., Phys. Rev. Lett. **92**, 225001 (2004).

[19] G. I. Taylor, Proc. R. Soc. London A **201**, 159 (1950).

[20] L. I. Sedov, Similarity and Dimensional Methods in Mechanics (Academic, New York, 1959).

[21] Y. B. Zeldovich and Y. P. Raizer, Physics of Shock Waves and High-Temperature Hydrodynamic Phenomen (Academic, New York, 1966).

[22] E. Liang and K. Keilty, Astrophys. J. (2000).

[23] C. F. McKee and J. P. Ostriker, Astrophys. J. **218**, 148 (1977).

[24] E. Cohen, T. Piran, and R. Sari, Astrophys. J. **509**, 717 (1998).

[25] P. Reinicke and J. M. ter Vehn, Phys. Fluids A **3**, 1807 (1991).

[26] R. T. Barton, in Numerical Astrophysics, ed. J. M. Centrella, J. M. LeBlanc, and R. L. Bowers (Jones and Bartlett, Boston, 1985).

[27] A. D. Edens, T. Ditmire, J. F. Hansen, M. J. Edwards, R. G. Adams, P. Rambo, L. Ruggles, I. Smith, and J. L. Porter, Physics of Plasmas, accepted (2004).

[28] G. B. Zimmerman and R. M. More, J. Quant. Spectrosc. Radiat. Transfer **23**, 517 (1980).

[29] G. B. Zimmerman and W. L. Kruer, Comments Plasma Phys. Controlled Fusion **2**, 51 (1975).

[30] D. Mihalas and B. W. Mihalas, Foundations of Radiation Hydrodynamics (Oxford University Press, Oxford, 1984).

[31] S. P. Hatchett, Tech. Rep., Lawrence Livermore National Laboratory, CA (1991), uCRL-JC-108348: Ablation Gas Dynamics of Low-Z Materials Illuminated by Soft X-Rays. Copies may be obtained from the National Technical Information Service, Springfield, VA 22161.

[32] G. I. Barenblatt, Similarity, Self-Similarity and Intermediate Asymptotics (Consultants Bureau, New York, 1979).

Study of high Mach number laser driven blast waves

A. D. Edens and T. Ditmire
Department of Physics, University of Texas at Austin, Austin, TX 78712

J. F. Hansen and M. J. Edwards
Lawrence Livermore National Laboratory, Livermore, CA, 94550

R.G. Adams, P. Rambo, L. Ruggles, I.C. Smith, and J. L. Porter
Sandia National Laboratories, Albuquerque, NM, 87059

Abstract

The study of blast waves produced by intense lasers in gases is motivated by the desire to explore astrophysically relevant hydrodynamic phenomena in the laboratory. A systematic scan of laser produced blast waves was performed and the structure of blast waves was examined over a wide range of drive laser energy. Lasers with energies ranging from 10J-1000J illuminated a pin target in either xenon or nitrogen gas, creating a spherical blast wave. A strongly radiating blast wave in xenon gas is observed while blast waves in nitrogen more closely approximate a pure Taylor-Sedov wave. It is also found that at all laser energies, blast waves traveling through xenon gas had their hydrodynamic evolution significantly affected by the passage of the illumination laser.

PACS number: 52.35.Py, 52.38.-r, 52.72.+v

I. Introduction

The stabilty of blast waves has been a long standing problem of interest in the physics and astronomy communities [1,2]. In particular, there are several instabilities associated with the formation and evolution of supernova remnanta (SNRs)[2-4]. One important hydrodynamic feature, an overstability proposed by Vishniac *et al.* about 20 years ago [5], arises from a mismatch between the ram and thermal pressures at the surface of a blast wave which can cause a growing, oscillating ripple on that surface. The growth rate of the overstability depends mainly on two factors, the wavelength of the perturbation and the thickness of the blast wave, which is determined by the gas' adiabatic index[5]. Energy losses through radiation make a strongly radiating blast wave cooler and thusly more compressible, leading to a thinner blast wave which is susceptible to the Vishniac overstability. Therefore the Vishniac overstability may be responsible for the large scale structure seen in some radiative SNRs[2,6] , and may also play a role in the formation of stars [3,7].

There have been various experimental and computation studies attempting to confirm the existence and growth rates of the Vishniac overstability. Blondin *et al.* conducted a series of 1-D and 2-D radiative hydro simulations which appeared to confirm the existence of the overstability [6]. MacLow and Norman conducted 2-D simulations where they confirmed the theoretical growth rates for the overstability assuming the

amplitude of the perturbation does not get large compared to the radius of the blast wave[8]. In addition, over the previous fifteen years there have been a number of experimental attempts to observe the overstability [9-11]. These experiments have produced their blast waves chiefly through the creation of an explosion by irradiation of a target by a high-powered laser pulse. In these laser experiments the laser delivers a large quantity of energy in a small focal spot over a time period short compared to the evolution time of the resulting blast wave. A short intense point explosion is also how one would describe a supernova on astrophysical scales, making laser driven explosions well suited to studying similar physics.

Important early experimental work was published by Grun *et al.* [9], using the Pharos III laser at the Naval Research Laboratory. They conducted experiments on the evolution of hemispherical blast waves produced in a background gas by single-sided irradiation of a foil by 200J laser pulses. Grun *et al.* reported observing the Vishniac overstability grow from noise in blast waves traveling through xenon gas back upstream of the incoming laser, while those blast waves traveling through nitrogen gas remained stable and the shock front remained smooth. However, whereas theory predicted a maximum growth rate going as $t^{0.7}$ at an _ number of ~50, Grun *et al.* observed[9] growth going as $t^{1.6}$ at an _ number of ~10.

More recent work on cylindrical laser produced blast waves in Xe driven by an ultra-fast laser was published by Edwards *et al.*[10]. They observed evidence of the formation of a radiative shock but did not observe any perturbation growth on the shock front. The authors postulated the reason they saw no growth was that the Mach number of their blast wave was too low and that the wave was heated by efficient electron conduction between the hot core and the blast wave shell, leading to a higher effective adiabatic index and a thicker blast front. Theoretical work by Lamming et. al.[12] seemed to confirm this idea by showing that there is a velocity cutoff for the overstability to affect blast waves traveling through xenon gas. However, Lamming *et al.* could not explain the discrepancy between theory and the NRL experiments in regards to the position and size of the maximal growth feature.

The velocity and temperature of a laser driven blast wave will increase with the increasing drive laser energy. Therefore, a systematic scan of laser energies should allow for a more comprehensive study of the overstability. In this letter we report on such a systematic examination of spherical blast waves produced by laser energies spanning two orders of magnitude, from 10J to 1000J. This scan produced blast waves in both nitrogen and xenon including blast waves in xenon both above and below the 25 km/s threshold for overstability growth predicted by Lamming *et al* [12]. We compare the results with theoretical simulations and the previous experimental work and find that laser pre-ionization of the surrounding gas can significantly affect the dynamics and morphology of these shock experiments. The effect is particularly pronounced for blast waves traveling through xenon gas.

II. Experimental Setup

A schematic of our experimental setup is shown in Fig. 1. A pump laser varying in energy from 10-1000J was focused into a target chamber filled with between 5 and 10 Torr of xenon or nitrogen gas. The laser illuminated one side of a ~0.5mm pin target of steel or nylon. This created an explosion that formed a blast wave in the surrounding gas. The use of a pin target (as opposed to the planar foil targets used in Grun's experiment[9])

allowed us to examine the evolution of the blast wave both in the gas previously traversed by the laser on the front side of the pin and in the pristine gas on the back side of the pin. Some variable time later a probe laser pulse was fired. This passed through our experimental region and was then imaged with a dark-field imaging telescope. This diagnostic, (illustrated in the inset of figure 1) is sensitive to gradients in plasma density and is therefore well suited to examining the interface region between the ionized blast wave shell and unionized gas. We characterized the shock radius and front morphology as the blast wave expanded by scanning the time delay between the pump and probe beams.

Our experiments were performed on two different laser systems. The first was the Janus laser at Lawrence Livermore National Laboratory[13]. This laser fired 1ns pulses with pulse energies between 10J and 150J at 1053nm. Here a 5mJ, 532nm beam gated to 2 ns probed the blast wave. We performed higher laser drive energy experiments on the Z-Beamlet laser at Sandia National Laboratories[14]. This laser fired 1 ns pulses, with 527 nm wavelength at energies between 500J and 1000J. The probe beam on these experiments was a ~150ps beam with 10s of mJ at 1064nm.

III. Data and Analysis

We have evidence that shock waves in Xe were strongly radiative at early times for the highest energy shots we conducted. First we observe a radiative precursor in front of the blast wave. This precursor takes the form of a "glow" ahead of the shock wave in the data reproduced in Figure 3 (described below). This glow was confirmed through the use of interferometry in which a region of increasing electron density was observed preceding the shock front. This precursor was seen for blast waves traveling through xenon at all energies, but in nitrogen the precursor was only observed for the highest laser energy shots. For the highest energy blast waves in xenon, the precursor extended off the field of view of the camera, which meant the precursor extended for several centimeters in all directions around the wave. However, this precursor wave only demonstrated that there was radiation coming from the blast waves, not that it was affecting the dynamics of the wave's evolution. To gauge the impact of the radiation we looked at the blast wave trajectories.

A blast wave can be characterized by its asymptotic trajectory $R(t) = \beta t^{\alpha}$ where the deceleration parameter $\alpha = Vt/R$. Here V and R are the velocity and radius of the shock wave at time t after the explosion. In a classical spherical, energy conserving Sedov-Taylor wave consisting of a high pressure low density central core pushing a thin compressed shell, $a=2/5$ [15]. If the surrounding gas is sufficiently dense and radiative cooling is important, the deceleration parameter falls below the Taylor Sedov value and the rate of deceleration is faster than a purely energy conserving wave. When the thin shell of the blast wave is cooled efficiently by radiative losses α approaches *2/7*. In this so-called "pressure driven snowplow" regime the low density central core continues to exert pressure on a shell which cannot support itself and collapses to high density [16]. If radiative cooling of the hot low density core is also efficient, the pressure of the core becomes negligible, and the wave enters the "momentum conserving snow-plow" regime, in which $\alpha=1/4$[16]. We measured the radial trajectory of blast waves in both Xe and N_2 at all laser energies. The data for the 1000J shots are plotted in figure 2. We see that at late times, both Xe and N_2 blast waves follow the Taylor Sedov $t^{2/5}$ trajectory. This is

consistent with the trajectories observed by Grun *et al*[9]. However, at early time (t<200ns) the blast wave in Xe follows a trajectory with $\alpha = 1/4$. This lower α seems to suggest that the blast waves in our experiments go through a strongly radiative stage prior to 200ns.

Images of shockwaves traveling through 5-10 Torr of Xenon gas are shown on the left side of Fig. 3. The shockwaves were produced by a range of laser driver energies, 10J, 500J, and 1000J. In all cases the laser pulse came in from the left of the picture. All show similar behavior. There is a marked difference between the section of blast wave traveling over the gas region traversed by the laser and the rest of the blast wave on the back side of the pin. The difference is a turbulent region with a large perturbation of roughly wave number 10 on the laser side of the wave that is not present on the back side of the wave. This feature is consistent in position and wave number with the Grun results[9]. The turbulent feature we see becomes increasingly pronounced with increasing energy, but the qualitative behavior is similar. However, there are smaller scale perturbations, closer in wave number to the theoretical maximal growth rate region, that appear only at higher energies. Though it is difficult to measure a growth rate for these perturbations due to their small size, they seem more consistent with the Vishniac overstability and are seen both in our higher energy data and in the data from Grun *et al*[9]. The xenon images can be contrasted with the images of blast waves traveling through 5-10 Torr nitrogen gas, shown on the right side of the same figure. Again we see blast waves produced by the same three laser drive energies. In this case the feature seen in xenon in the region traversed by the laser is greatly reduced and the small scale perturbations never arise. The fact that a qualitatively energy independent feature is seen only on blast waves traveling through Xenon and only on the side of the blast wave that interacted with the laser suggests that there is some effect of the laser's passage on the evolution of blast waves in xenon. This feature is evident both at low and high energy and with 1053 nm and 527 nm laser drive pulses.

We attribute this turbulent feature in Xe to pre-ionization of the gas by the laser. The most likely reason that the feature is seen on blast waves traveling through xenon gas and not on those traveling through nitrogen gas has to do with the different multi-photon ionization thresholds of these gasses. The threshold for multi-photon ionization in xenon is lower than in nitrogen. At 527nm ionization is a 5 photon process in xenon, as compared to 7 in nitrogen, and the ratio increases for higher charge states. This means that there is likely more ionization and heating of the xenon gas caused by the laser's passage, creating a low gas density region. Therefore, the blast wave traveling over this area will pick up gas that is lower density and hotter than in other regions, causing it to slow down less as it travels, creating the bump like feature seen. In both our results and Grun *et al*.'s [9] the feature appears in the laser cone path, as is illustrated in the 1st panel of Fig. 3. If the feature were associated with the Vishniac overstability, one would expect rippled features at all points on the spherical blast shell, depending on random noise in the background gas and the initial blast wave. The feature also appears independent of the blast wave velocity. In our shots the average velocity at early times (between 50 ns and 100 ns) ranges from ~12 km/s for 10J shots, below the 25 km/s threshold predicted for the onset of the overstability in xenon gas predicted by Lamming [12], to ~140 km/s for the 1000J shots, above this threshold. These facts support the idea that the feature is caused by the laser's passage.

IV. Simulations

We have performed simulations that support and further clarify the conclusions suggested by the data. We performed 2D simulations of blast wave evolution using the Lawrence Livermore National Laboratory code CALE [17]. CALE is a 2-D arbitrary Lagrangian Eulerian (ALE) code with a tabular equation of state (EOS) and interface tracking. For our simulations we assumed ~7.5 Torr of xenon gas for the initial background. A 0.5mm Mo sphere was used as the target and the laser pulse was 100J in 5ns, with a 0.4mm focal spot size. Some results from the simulation are shown in Figure 4. The first panel of the figure shows a contour plot of the electron temperature 17ns after the initial laser pulse. One can clearly see the hot plasma in the region of the laser cone. The second panel of the figure shows simulated density gradients of a blast wave traveling through 7.5 Torr of Xenon gas about 400 ns after the 100J drive beam struck the target. Finally the 3rd panel shows experimental data taken at t=300ns and 10J drive. There is a strong similarity between the experimental result and the simulation. The large perturbation on the blast wave's surface in the simulation is qualitatively similar to that seen in all our xenon experimental results and to that seen in previous experiments[9]. While the large perturbation on the blast wave surface does show up, the smaller scale structure seen on the blast waves in xenon produced by high energy shots is absent. This is most likely due to inadequate resolution of the experiments. The simulation uses 4 degree angular zoning which is adequate to start to see the affects of the laser channel on the evolving blast-wave, but is much too coarse to resolve the small scale "turbulent" features seen in the experiment. These small scale features, which are almost certainly 3D, evidently evolve differently in the case of Xe, and may be indicative of the higher compressibility of Xe through ionization and or radiative effects. It may well prove instructive to examine this possibility computationally in future, but the 3D nature of the flow makes this a formidable task.

V. Conclusions

In conclusion, we have performed a systematic examination of shockwaves traveling through 5-10 Torr of either xenon or nitrogen gas as a function of laser energy. Strongly radiative blast waves form at early time for high energy drive beams in Xe, which produce a large radiative precursor ahead of the shock and which decelerate much faster than a Sedov energy conserving wave. We have also observed a striking feature that appears at all drive laser energies in xenon gas corresponding to the region where the drive laser had previously traveled. This appears to result from a heating and ionization of the gas in this area by the laser. A warm, low density channel is created in which the blast wave will travel at higher velocities than in other regions of the gas. Our experimental results are supported by simulations. This result may explain the experimental deviation with theoretical calculations seen in previous results[9,12], where the maximal growth rate was seen at a different wavelength than expected and was larger than expected. The maximal growth rate feature appears to be produced by the laser's passage and is not a result of the Vishniac overstability. However, there is a large amount of small scale structure that appears at only the higher energy shots and only in xenon. This structure is more consistent with the Vishniac overstability, but difficult to measure a growth rate for due to the small spatial scales. These results suggest that caution must be exercised when interpreting hydrodynamic effects in laser driven

experiments in gas traversed by a laser pulse. There are several complicated interactions that can arise, especially in a gas that is easily ionized, like xenon.

VI. Acknowledgements

Refrences

[1]   J. J. Erpenbeck, Physics of Fluids **5** (10), 1181 (1962).
[2]   P.A. Isenberg, Astrophysical Journal **217** (2), 597 (1977).
[3]   G. L. Welter, Astronomy and Astrophysics **105** (2), 237 (1982); G. Welter and J. Schmidburgk, Astrophysical Journal **245** (3), 927 (1981).
[4]   C. F. Mckee and B. T. Draine, Science **252** (5004), 397 (1991); J. P. Ostriker and C. F. Mckee, Reviews of Modern Physics **60** (1), 1 (1988).
[5]   E. T. Vishniac, Astrophysical Journal **274** (1), 152 (1983); D. Ryu and E. T. Vishniac, Astrophysical Journal **368** (2), 411 (1991); D. Ryu and E. T. Vishniac, Astrophysical Journal **313** (2), 820 (1987).
[6]   J. M. Blondin, E. B. Wright, K. J. Borkowski et al., Astrophysical Journal **500** (1), 342 (1998).
[7]   B. G. Elmegreen and D. M. Elmegreen, Astrophysical Journal **220** (3), 1051 (1978); B. G. Elmegreen and C. J. Lada, Astrophysical Journal **214** (3), 725 (1977).
[8]   M. M. MacLow and M. L. Norman, Astrophysical Journal **407** (1), 207 (1993).
[9]   J. Grun, J. Stamper, C. Manka et al., Physical Review Letters **66** (21), 2738 (1991).
[10] M. J. Edwards, A. J. MacKinnon, J. Zweiback et al., Physical Review Letters **8708** (8), art. no. (2001).
[11] T. Ditmire, K. Shigemori, B. A. Remington et al., Astrophysical Journal Supplement Series **127** (2), 299 (2000); K. Shigemori, T. Ditmire, B. A. Remington et al., Astrophysical Journal **533** (2), L159 (2000).
[12] J. M. Laming and J. Grun, Physical Review Letters **89** (12) (2002); J. M. Laming and J. Grun, Physics of Plasmas **10** (5), 1614 (2003).
[13] J.A. Glaze, W.W. Simmons, and W.F. Hagen, *Status of large neodymium glass lasers*. (Soc. Photo-Optical Instrumentation Engrs, Palos Verdes Estates, CA, USA
Reston, VA, USA, 1976).

[14]   ; J. L. Rambo P. K. Rambo, Jr., G. R. Bennett, I.C. Smith, A.C. Erlandson, J.E. Murray, and J. Caird, OSA Trends in Optics and Photonocs, Conference on Lasers and Electro-Optics **73**, 362 (2002).

[15]   I. A. B. Zel*dovich, I. U. P. Raizer, Wallace D. Hayes et al., *Physics of shock waves and high-temperature hydrodynamic phenomena*. (Academic Press, New York,, 1966).

[16]   E. Cohen, T. Piran, and R. Sari, Astrophysical Journal **509** (2), 717 (1998).

[17]   *CALE Users Manual*. (Lawrence Livermore National Laboratory, 1991).

Figure Captions

FIG. 1: Experimental setup of laser shock experiments. Drive beam, varying in energy from 10J-1000J, enters the chamber from left and illuminates a pin target. This creates a blast wave that is imaged by the probe laser onto a dark field imaging telescope, shown in the inset. The dark field telescope blocks light that passes through the chamber undeflected, but any light that encounters a density gradient is deflected around the beam block at the center of the telescope and shows up as a bright area.

Figure 2: Blast wave trajectory through xenon and nitrogen gas. After ~200 ns in xenon the trajectory changes from $t^{0.25}$, indicative of a highly radiative blast wave, to $t^{0.4}$, consistent with the energy conserving Taylor-Sedov solution. The nitrogen blast wave trajectory is always consistent with the Taylor-Sedov solution. The error bars in the figure are smaller than the data points.

Figure 3: Dark-field images of blast waves traveling through xenon (left) and nitrogen (right) gas produced by various drive laser energies. In all cases drive laser enters from left. From top to bottom drive laser energies are ~10J, ~500J, and ~1000J. There is a contrast both in the small scale structure and the laser-side feature between the gasses.

Figure 4: Panel a has a simulation of the electron temperature (in keV) 17ns after a 100J laser pulse struck a pin target. Panel b is a comparison of simulated and experimental blast wave shapes. The simulation is 400ns after a 100J laser pulse. The experiment shows a blast wave 300ns after a 10J shot.

Blast Wave

<100mJ, <2ns Probe beam

Pin Target

10-1000J, ~1ns Drive Beam

C C D

Beam Block

F1

F2

Xenon   Nitrogen

Laser In

0.5cm

10J, 300ns   10J, 50ns

500J, 500ns   500J, 600ns

1000J, 400ns   1000J, 500ns

a

1 MM

Laser Cone

Target

12 eV
10
8
6
4
2 eV
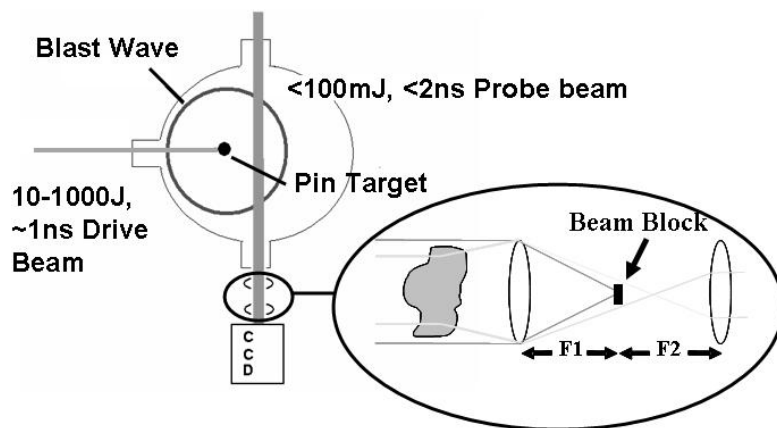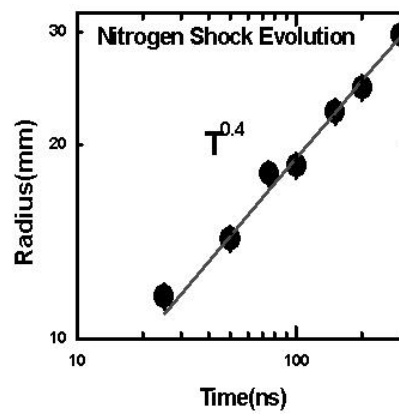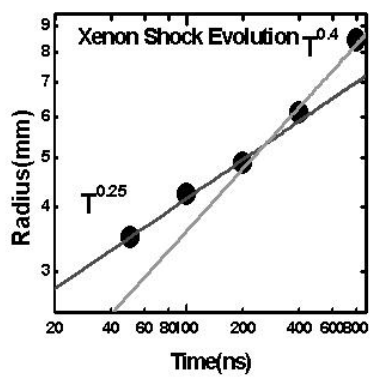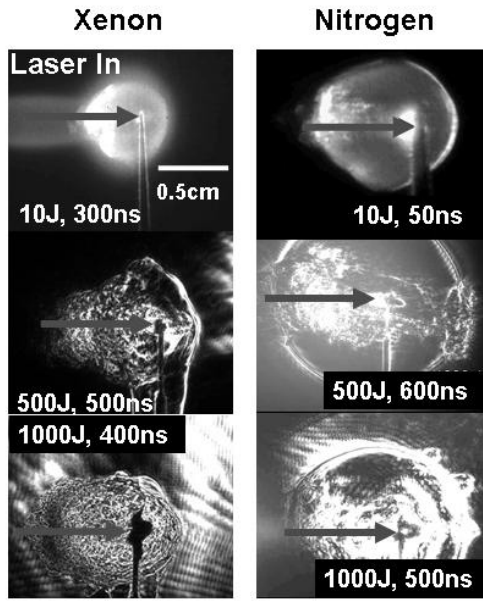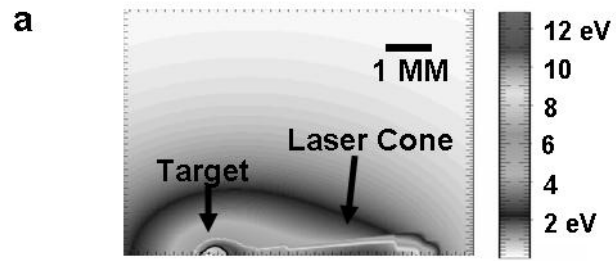
Experiment

Simulation

b

5 MM

Laser Cone
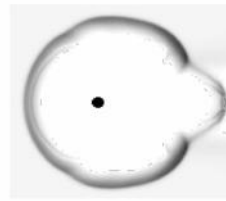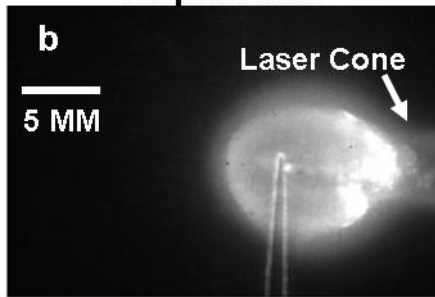
Appendix 4

Other blast wave interactions

A4.1 Blast wave foam interactions

While design and numerical simulations of a new gas injection system was under way, we also tried having blast waves interact with low density solids (aerogels) and have one blast wave interact with another. The hope with the aerogel experiment was that preheat would turn the solid aerogel into a gas prior to shock wave arrival. To achieve this, the strongest possible shocks were needed, so we limited shot operations to only full energy system shots, taking the penalty of a much longer laser cool-down time, and a relatively limited number of total shots. In this experiment, blast waves still originated at the laser focus on a stainless steel pin, and each aerogel sample was mounted in an annular metal holder facing the pin, initially at a distance of 20.0 mm from the pin. We did not observe the aerogel gasify, and reduced the aerogel to pin distance to 11.2 mm. In this configuration we could clearly see the aerogel shooting out from its ring-shaped holder (see Fig. A4.1), but it still appeared solid. We reduced the separation distance to the minimum possible, 4.0 mm, resulting in the shock-aerogel interaction fragmenting the aerogel which shot out as small shards, presumably solid, through the back of the holder. All of the aerogel experiments were done using nitrogen as the ambient gas. The gas pressure was p=5.3 kPa, just below the limit where laser focusing breaks down the gas. It's possible that using xenon as the ambient gas would have worked better, if radiation from the shock would turn the solid aerogel into a gas prior to the hydrodynamic interaction, but we did not have enough laser time or aerogel targets to investigate this. Another experimental difficulty with this experiment is the need to open the target vacuum chamber between each shot to replace the aerogel (the stainless steel pin does not have to be replaced more than every few system shots, or dozens of low-energy rod shots). This means replacing the entire chamber atmosphere each shot, which is more expensive when using xenon than nitrogen.
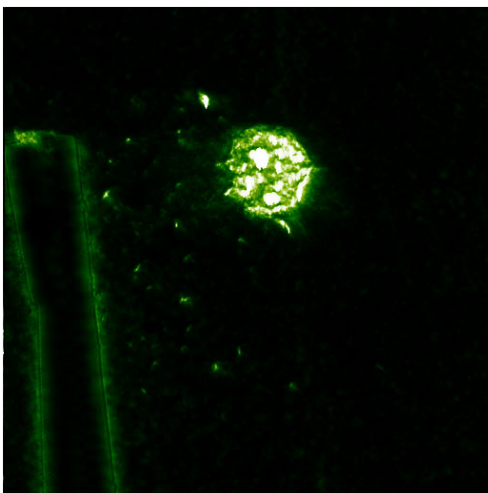
Figure A4.1. Schliern image of aerogel being launched out of its holder by the blast wave incident from the left. The foam appears to be still largely in tact.

A4.2 Double blast wave experiments

By using both legs of the Janus laser facility and shooting at two target pins, we created to blast waves simultaneously and had them interact with one another (see Fig. 4.2). We created one blast wave with more energy than the other, so that the one with more energy would roll over the smaller one. This proved partially successful in that the interaction between the two blast waves displayed turbulent features (and also Mach stems), but due to the nature of blast wave scaling where the expansion velocity quickly drops ($v \sim r^{-3/5}$), even the maximum energy of a full system shot ($E \sim 150$ J) was not sufficient for the larger blast wave to completely pass over the smaller one. By introducing small timing delays and giving the larger wave a head start, the blast wave scaling law could be compensated for somewhat, but in reality larger energy contrast ratios are needed from the facility and this was not pursued further
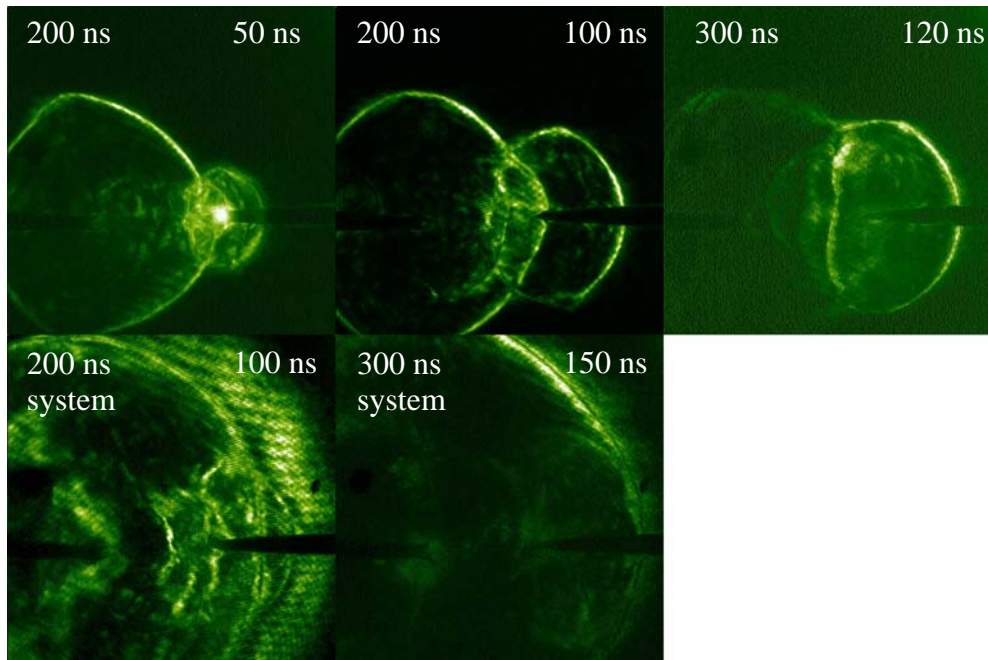
Figure A4.2. Interacting blast waves. The upper three images each show two blast waves created with similar energies ($E \sim 4$ J) partially passed across each other. Note how the low density and high sound speed inside a blast wave lets the other blast wave move faster, and how the intersecting interior is turbulent. The two lower images show the same features but here the left hand side blast wave is created with higher energy ($E \sim 100$ J) which, coupled with a head start as indicated by the time numbers, allows it to almost completely pass over the smaller wave.